AGU PUBLICATIONS

JGR

Journal of Geophysical Research: Planets

RESEARCH ARTICLE
10.1002/2016JE005095

Key Points:
- We have developed a stratigraphy for lower Mount Sharp using analyses of new spectral, thermophysical, and morphologic orbital data products
- Siccar Point group records a period of deposition and exhumation that followed the deposition and exhumation of the Mount Sharp group
- Late state silica enrichment and redox interfaces within lower Mount Sharp were pervasive and widespread in space and/or in time

Correspondence to:
A. A. Fraeman,
abigail.a.fraeman@jpl.nasa.gov

Citation:
Fraeman, A. A., B. L. Ehlmann, R. E. Arvidson, C. S. Edwards, J. P. Grotzinger, R. E. Milliken, D. P. Quinn, and M. S. Rice (2016), The stratigraphy and evolution of lower Mount Sharp from spectral, morphological, and thermophysical orbital data sets, *J. Geophys. Res. Planets*, *121*, 1713–1736, doi:10.1002/2016JE005095.

Received 1 JUN 2016
Accepted 26 AUG 2016
Accepted article online 30 AUG 2016
Published online 17 SEP 2016

The stratigraphy and evolution of lower Mount Sharp from spectral, morphological, and thermophysical orbital data sets

A. A. Fraeman[1], B. L. Ehlmann[1,2], R. E. Arvidson[3], C. S. Edwards[4,5], J. P. Grotzinger[2], R. E. Milliken[6], D. P. Quinn[2], and M. S. Rice[7]

[1]Jet Propulsion Laboratory, California Institute of Technology, Pasadena, California, USA, [2]Division of Geological and Planetary Sciences, California Institute of Technology, Pasadena, California, USA, [3]Department of Earth and Planetary Sciences, Washington University in St. Louis, St. Louis, Missouri, USA, [4]United States Geological Survey, Flagstaff, Arizona, USA, [5]Department of Physics and Astronomy, Northern Arizona University, Flagstaff, Arizona, USA, [6]Department of Earth, Environmental and Planetary Sciences, Brown University, Providence, Rhode Island, USA, [7]Geology Department, Physics and Astronomy Department, Western Washington University, Bellingham, Washington, USA

Abstract We have developed a refined geologic map and stratigraphy for lower Mount Sharp using coordinated analyses of new spectral, thermophysical, and morphologic orbital data products. The Mount Sharp group consists of seven relatively planar units delineated by differences in texture, mineralogy, and thermophysical properties. These units are (1–3) three spatially adjacent units in the Murray formation which contain a variety of secondary phases and are distinguishable by thermal inertia and albedo differences, (4) a phyllosilicate-bearing unit, (5) a hematite-capped ridge unit, (6) a unit associated with material having a strongly sloped spectral signature at visible near-infrared wavelengths, and (7) a layered sulfate unit. The Siccar Point group consists of the Stimson formation and two additional units that unconformably overlie the Mount Sharp group. All Siccar Point group units are distinguished by higher thermal inertia values and record a period of substantial deposition and exhumation that followed the deposition and exhumation of the Mount Sharp group. Several spatially extensive silica deposits associated with veins and fractures show that late-stage silica enrichment within lower Mount Sharp was pervasive. At least two laterally extensive hematitic deposits are present at different stratigraphic intervals, and both are geometrically conformable with lower Mount Sharp strata. The occurrence of hematite at multiple stratigraphic horizons suggests redox interfaces were widespread in space and/or in time, and future measurements by the Mars Science Laboratory Curiosity rover will provide further insights into the depositional settings of these and other mineral phases.

1. Introduction

Gale Crater is a ~150 km diameter impact crater located on the Martian dichotomy boundary. It was selected as the site for in situ exploration by the Curiosity Mars Science Laboratory (MSL) rover largely due to the presence of a ~5 km high stack of sedimentary rocks in the center of the crater, formally named Aeolis Mons and informally known as Mount Sharp [*Golombek et al.*, 2012; *Grotzinger et al.*, 2012]. The sedimentary nature of Mount Sharp was first observed in Mars Orbiter Camera images [*Malin and Edgett*, 2000], and hypotheses about the origin of the mound based on orbital data include lacustrine, aeolian, ice-mediated or air fall deposition, formation as a spring deposit, or some combination of the above [e.g., *Wray*, 2013, and references therein].

During the first ~1300 Martian days (sols) after landing, Curiosity crossed the plains of Gale Crater's floor and began to ascend the NW flank of Mount Sharp, characterizing sedimentary rocks within three stratigraphic groups along the way (Figure 1). Two of these groups, the Bradbury and Mount Sharp groups, comprise the oldest strata in Gale Crater [*Grotzinger et al.*, 2015]. Rover observations coupled with orbital mapping demonstrated the rocks of the Bradbury group were formed in a set of small fluvio-deltaic complexes adjacent to a predominately subaqueous, lacustrine system that deposited the Murray formation, the oldest Mount Sharp group rocks accessible to Curiosity [*Grotzinger et al.*, 2015; *Stack et al.*, 2016]. The third stratigraphic group, first named here as the Siccar Point group, visited by Curiosity is a younger group that truncates and unconformably overlies the Mount Sharp group [*Grotzinger et al.*, 2015; *Banham et al.*, 2016; *Watkins et al.*, 2016].

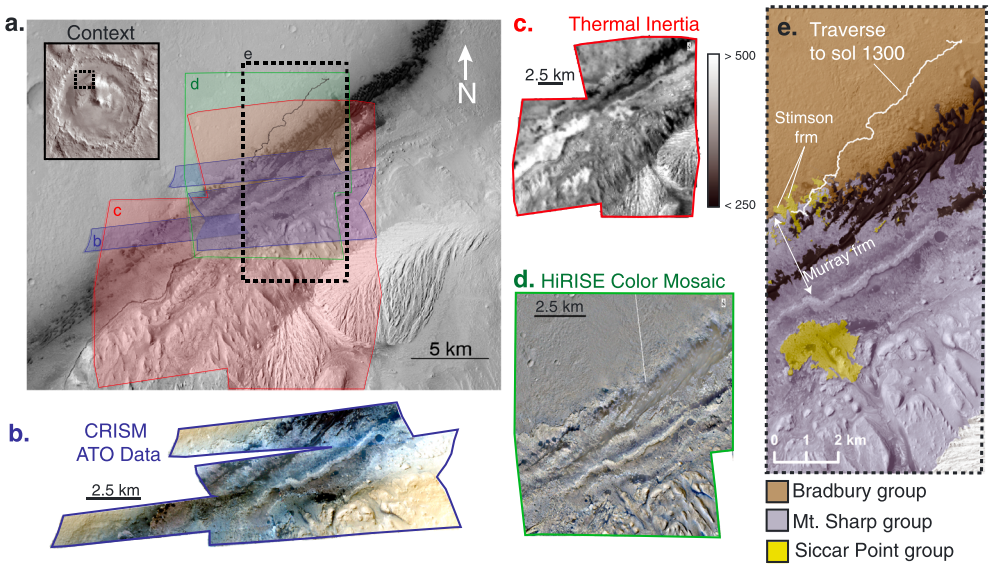

Figure 1. (a) CTX mosaic of study area over lower Mount Sharp. Footprints of new derived data products are shown outlined in (b) blue (CRISM ATO data, stretched color shown R: 0.6 μm, G: 0.53 μm, B: 0.44 μm), (c) red (THEMIS TI), and (d) green (HiRISE color mosaic). These derived products are integrated with existing CRISM, HiRISE, and CTX data products. (e) Detail of Curiosity's traverse to sol 1300 and previously defined stratigraphic groups. After *Grotzinger et al.* [2015].

Studies of Mount Sharp using Context Camera (CTX) and High-Resolution Imaging Science Experiment (HiRISE) orbital data sets, coupled with mineralogical information from the Observatoire pour la Minéralogie, l'Eau, les Glaces et l'Activité (OMEGA) and Compact Reconnaissance Imaging Spectrometer for Mars (CRISM), show variability in the texture and composition of Mount Sharp group strata. Consistent stratigraphic relationships are at times traceable for tens of kilometers on Mount Sharp's NW flank [*Anderson and Bell*, 2010; *Milliken et al.*, 2010; *Thomson et al.*, 2011; *Fraeman et al.*, 2013; *Le Deit et al.*, 2013]. The strata record periods of geochemical and environmental changes that can be further evaluated by the Curiosity rover. Understanding the extent to which patterns in primary deposition versus patterns of overprinting diagenesis were responsible for observed textural and compositional changes will be crucial for reconstructing past surface and burial environments that existed in Gale Crater. Mount Sharp may have once been partially or completely buried [*Malin and Edgett*, 2000], and a higher early Martian geothermal gradient permitted peak temperatures at the base of Mount Sharp to have been warm enough to sustain diagenetic fluids [*Borlina et al.*, 2015]. Orbital and Curiosity data also both present abundant evidence for early and late-stage diagenetic aqueous processes, including a variety of concretions associated with Mg-Fe smectite clay-bearing mudstones, sedimentary dikes and other fluid and gas escape features, sulfate-filled veins, and fracture-associated silica-rich halos throughout the lower Mount Sharp [*Anderson and Bell*, 2010; *Leveille et al.*, 2014; *Nachon et al.*, 2014; *Siebach and Grotzinger*, 2014; *Siebach et al.*, 2014; *Stack et al.*, 2014; *Vaniman et al.*, 2014; *Grotzinger et al.*, 2015; *Kronyak et al.*, 2015].

Detailed orbital-based maps are key tools for contextualizing Curiosity's observations as it continues to explore the NW flank of Mount Sharp and for time-ordering events in the evolution of Mount Sharp. Here we use newly derived, highest resolution orbital data and coanalysis of integrated data sets from three instruments (CRISM, HiRISE, and the Thermal Emission Imaging System (THEMIS)), to generate detailed maps of lower Mount Sharp and a stratigraphic section of key units. We incorporate previous observations [*Anderson and Bell*, 2010; *Milliken et al.*, 2010; *Thomson et al.*, 2011; *Fraeman et al.*, 2013; *Le Deit et al.*, 2013] while using new orbital data products to discriminate meter-scale features. Nine discrete units are identified based on combined analysis of color, textural, compositional, thermophysical, and three-dimensional stereo data. Based on these units and their inferred stratigraphic relationships, we generate hypotheses for aspects of Mount Sharp's formation and evolution that are locally testable by in situ measurements from parts of the map area Curiosity will explore.

Table 1. Orbital Data Sets Used in This Study

Instrument	Scene ID	Spatial Resolution	Wavelength Coverage
HiRISE	ESP_028823_1755	25 cm/pixel	0.53–0.86 μm
	PSP_009716_1755		
	ESP_036194_1755		
	ESP_035772_1755		
	ESP_021610_1755		
	ESP_033649_1750		
	ESP_022111_1755		
	PSP_009149_1750		
	ESP_027834_1755		
	ESP_029746_1755		
	ESP_029957_1755		
	ESP_032436_1755		
	ESP_030168_1755		
CRISM	HRL0000BABA	36 m/pixel	0.4–4.0 μm
	FRT0000B6F1	18 m/pixel	
	FRT0001BBA1		
	ATO00021C92	12 m/pixel	
	ATO0002EC79		
	ATO00038AA7		
THEMIS	I17950012	100 m/pixel	6.78 μm–14.88 μm

2. Orbital Data Products and Methods

We generated orbital data mosaics of HiRISE color scenes (25 cm/pixel), CRISM along-track oversampled (ATO) images (12 m/pixel), and THEMIS IR data (100 m/pixel), described in detail below (Figure 1 and Table 1). We also utilized existing full resolution targeted (FRT) and half-resolution long (HRL) CRISM images (18 and 36 m/pixel, respectively) available from the Planetary Data System (PDS) and grayscale CTX (6 m/pixel) and HiRISE (25 cm/pixel) image basemaps with associated HiRISE digital elevation model (DEM) mosaics (up to 1 m/spacing) that cover the NW quadrant of Mount Sharp which were generated for the MSL project [*Golombek et al*., 2012]. The DEM mosaic was generated from 12 HiRISE stereo image pairs that were projected, georeferenced, and mosaicked to create a DEM with 1 m grid spacing and elevations tied to Mars Orbiter Laser Altimeter data [*Golombek et al*., 2012; *Calef et al*., 2013]. All data sets were merged into a geographic information system (GIS) framework for simultaneous, multidata set analysis.

2.1. HiRISE Color Mosaic

The HiRISE instrument on board the Mars Reconnaissance Orbiter (MRO) provides color information with a broadband filter centered at 694 nm and two narrower filters centered at 536 nm and 874 nm [*McEwen et al*., 2007]. Thirteen color HiRISE images (Table 1) covering an area ~11.8 × 10.5 km over lower northwest Mount Sharp (Figure 1d) were mosaicked together using a near-automated method designed for generating multiimage HiRISE mosaics [*Edwards et al*., 2011; *Oshagan et al*., 2014]. This mosaic was generated by orthorectification and georeferencing of the 13 HiRISE color images to a HiRISE grayscale basemap using both manually and automatically generated ground control points. Data from individual HiRISE detectors were normalized to account for intradetector variations, and individual images were normalized to one another to account for variations in illumination effects due to regional topography, viewing geometry, and atmospheric conditions. Finally, data were stretched using a running histogram stretch that maximizes the dynamic range on ~5000 × 5000 pixel segments (~km scale) of the image and removes additional regional variations [*Edwards et al*., 2011].

2.2. CRISM Data Products

CRISM is an imaging spectrometer that collects radiance from the Martian surface in 544 discrete wavelength channels from 0.35–3.9 μm [*Murchie et al*., 2007]. The CRISM optical bench is mounted on a gimbal that slews in the direction of MRO's orbit to account for along-track motion in the field of view and to allow for longer integration times and higher signal-to-noise ratios in collection of a high spatial resolution data set [*Murchie et al*., 2007]. When operating in full resolution targeted (FRT) mode, the angular velocity of the gimbal is set such that the instrument collects pixels having an 18 m footprint approximately every 18 m. The resulting FRT

image cubes have spatial resolutions of ~18 m/pixel projected on the surface. CRISM can also operate in an along-track oversampled mode (ATO) where the angular velocity of the gimbal is reduced so that the 18 m pixels are spaced less than 18 m apart in the along-track direction [*Fraeman et al*., 2013; *Arvidson et al*., 2014b; *Kreisch et al*., 2015]. The resulting overlap of pixels can be used to process the scene to spatial resolutions < 18 m/pixel. A third type of CRISM data product is a half-resolution long (HRL) image where pixels are spaced ~36 m in the along-track direction. The advantage of HRL products is that they provide greater spatial coverage than FRT and ATO scenes. We utilize data from all three of these observing modes (Table 1).

In this work, CRISM data are photometrically corrected by dividing each spectrum by the cosine of the incidence angle (assumes the Martian surface is approximately Lambertian). CRISM data are also atmospherically corrected using the "volcano scan" method, which approximates the atmospheric transmission spectrum using observations close in time to the CRISM observation of interest collected from the top and bottom of Olympus Mons [*McGuire et al*., 2009; *Murchie et al*., 2009]. Finally, CRISM data were coregistered to a HiRISE basemap using the geometric information associated with each CRISM cube and warped to the orthorectified basemaps using hand selected tie points.

Techniques that have been used to detect the weak spectral features on lower Mount Sharp using CRISM data include the standard approaches of generating parameter maps to mathematically highlight subtle spectral changes [*Pelkey et al*., 2007; *Viviano-Beck et al*., 2014], ratioing spectra from areas of interest to spectrally bland (dusty) material, averaging 10 s–100 s of spectra over large spatial areas, and processing CRISM data with noise-filtering algorithms [*Milliken et al*., 2010; *Fraeman et al*., 2013; *Seelos et al*., 2014]. Two additional methods designed to reduce noise in the CRISM data set and to aid in locating the small-scale outcrops that correlate with spectral signatures were also utilized in our work and are described below.

2.2.1. Regularization of Along-Track Oversampled Images in the Spectral and Spatial Domains Using Log-Likelihood Method With Penalty Function

Three CRISM ATO scenes collected over lower Mount Sharp (Figure 1b and Table 1) were regularized simultaneously in the spatial and spectral dimensions to 12 m/pixel spatial resolution using an iterative log maximum likelihood method with a log hyperbolic cosine penalty function regularization approach to return scene radiance data in the presence of noise [*Kreisch et al*., 2015]. Briefly, this method models the radiance of each pixel at each wavelength in a CRISM scene as $\mu = \boldsymbol{ABc}$ where μ is the blurred image cube, $\boldsymbol{A}$ and $\boldsymbol{B}$ are the spectral and spatial transfer functions, and c is the true radiance of the Martian scene. We invert this equation to retrieve a best estimate for c in the presence of Poisson noise using the maximum log-likelihood method and knowledge of the instrument spatial and spectral transfer functions that were characterized before launch and estimated using knowledge of instrument optics [*Murchie et al*., 2007]. A full description of the methodology and model validation can be found in *Kreisch et al*. [2015].

2.2.2. End-Member Similarity Maps

A library of scene-based spectral end-members was derived from regions within each CRISM observation (hematite, sulfates, clays, and hydrated materials) that were identified in previously published work [*Milliken et al*., 2010; *Fraeman et al*., 2013; *Seelos et al*., 2014]. These end-members were used to locate similar pixels in CRISM FRT scenes, which were determined by calculating the Euclidean distance between every spectrum in a scene and each end-member. All spectra were normalized to one at a reference wavelength to reduce effects of overall albedo variations, and when appropriate, comparisons were focused on wavelength regions where diagnostic absorption features are present and where the CRISM detector has the best signal to noise [*Murchie et al*., 2007]. The resulting maps sometimes highlight likely detections of these phases that are less noisy and more consistent between CRISM scenes as compared with standard CRISM parameter mapping.

2.3. Thermal Inertia Derivation

Thermal inertia (TI) is a function of material properties and is defined as $I = \mathrm{sqrt}(k\rho c)$, where k is the bulk thermal conductivity, ρ is the material density, and c is the heat capacity. On Mars thermal inertia is strongly controlled by the thermal conductivity which can be used to quantitatively determine the physical properties of the upper few skin depths of the observed surface [*Kieffer et al*., 1973; *Jakosky*, 1986; *Presley and Christensen*, 1997a, 1997b; *Piqueux and Christensen*, 2011]. To first order, fine, loosely consolidated material, such as dust, has low thermal inertias ($<100\ \mathrm{J\,K^{-1}\,m^{-2}\,s^{-1/2}}$), whereas well-cemented sedimentary rock ($>350\ \mathrm{J\,K^{-1}\,m^{-2}\,s^{-1/2}}$) or crystalline igneous rocks ($>1200\ \mathrm{J\,K^{-1}\,m^{-2}\,s^{-1/2}}$ [*Edwards et al*., 2009]) have higher thermal inertias. Martian

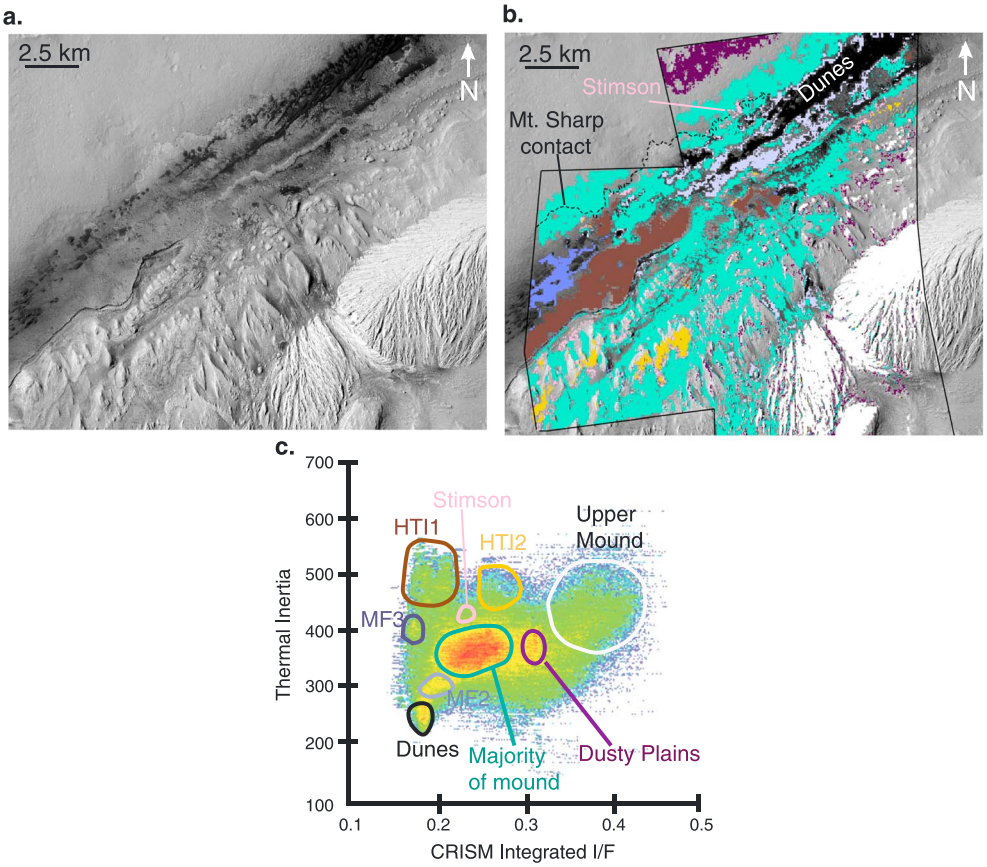

Figure 2. Relationship between albedo and thermophysical properties. Albedo is calculated from integrating cos i-corrected I/F CRISM values between 0.4 and 2.5 μm. (a) Mount Sharp context map, (b) spatial locations of regions with distinct albedo/TI relationships corresponding to (c) circled regions.

TI values are typically derived from THEMIS orbital data by fitting a Planck function to observed THEMIS radiance at 12.57 μm and then employing a lookup table to convert brightness temperatures to TI using the KRC thermal model which considers factors such as surface albedo, atmospheric opacity, observing geometry, orbital conditions, local time, and season [*Fergason et al.*, 2012; *Kieffer*, 2013]. To reduce uncertainties and improve accuracy in TI calculations over Gale Crater, we take into account the significant elevation changes and albedo variations in lower Mount Sharp throughout our study region, inputting pixel-specific values for albedos, slopes, slope azimuths, elevations, and lat/lons into the KRC thermal model to generate a unique T to TI lookup table for every THEMIS pixel in contrast to previously employed methods that rely on regional-scale values [*Fergason et al.*, 2012]. Albedo was derived from THEMIS VIS [*Edwards et al.*, 2011]; data and slope, azimuth, and elevation values were obtained from a CTX-DEM mosaic generated by the MSL project resampled to native THEMIS 100 m/pixel resolution. The resulting TI values show no correlations with elevation or albedo (Figure 1c).

3. Coordinated CRISM-TI-HiRISE Comparisons

Coregistered CRISM and TI data sets show that albedo, spectral, and thermophysical properties are related throughout the lower mound and in many cases covary with textural and geomorphic properties observable in HiRISE data (Figure 2). Most of the Mount Sharp group falls within a TI range of 300–400 $J\,m^{-2}\,K^{-1}\,s^{-1/2}$ and have CRISM albedos ranging from 0.2 to 0.3, although several spatially coherent end-members are apparent outside these ranges (Figure 2c).

One end-member (HTI1) is defined by its high thermal inertia and overall low-integrated I/F values. This end-member is morphologically distinguishable by its greater number of preserved craters, and it was mapped as

part of the "mound-skirting unit" in *Anderson and Bell* [2010] and part of the "unnamed draping strata" in *Grotzinger et al*. [2015]. While not an end-member in the integrated I/F versus TI scatterplot, the Stimson formation, which is also part of the unnamed draping strata in *Grotzinger et al*. [2015] and recently mapped in detail using Curiosity data [*Watkins et al*., 2016], is also distinct from the majority of Mount Sharp due to its higher thermal inertia and slightly brighter integrated I/F values. A second end-member unit (HTI2), characterized by equally high thermal inertia values but higher integrated I/F values, is also present on Mount Sharp.

The Bagnold dune field located at the base of Mount Sharp has lower thermal inertia and overall lower integrated I/F values than Mount Sharp bedrock. Additionally, several regions with distinct TI and albedo properties occur within the lower layers of Mount Sharp (MF2 and MF3). Finally, both the dusty plains Curiosity first traversed and the strata of the upper mound are distinct in the TI versus albedo space by their brighter CRISM-integrated I/F and higher thermal inertia in the case of the upper mound.

4. Orbital Unit Mapping

Incorporating results from this study and previous Mount Sharp mapping efforts [*Anderson and Bell*, 2010; *Milliken et al*., 2010; *Fraeman et al*., 2013; *Grotzinger et al*., 2015], we divide the lowest exposed layers into nine major units that are each characterized by a unique combination of texture, albedo, secondary mineralogy, and thermophysical properties (Figures 3 and 4 and Table 2). We use the term "unit" rather than a specific lithostratigraphic term such as "member," "formation," etc., because specific depositional process and relationships are difficult to infer from orbital data alone. Orbitally defined units may or may not have a common formation process, temporal relationship, or substantial thickness [e.g., *Grotzinger and Milliken*, 2012; *Stack et al*., 2016]. However, by choosing to define units using these hybrid attributes, we highlight terrains in the mound that differ from one another in physical properties [e.g., *Arvidson et al*., 2014a] and compositions, both of which could reflect variations in depositional conditions and postdepositional alteration histories that will be more fully characterized with Curiosity data.

Four of the units (HTI1, HTI2, MF2, and MF3) are defined principally based on their position in TI versus albedo space (Figure 2), and their specific boundaries were determined by examining high spatial resolution HiRISE color and grayscale images. The remaining five units (Murray formation 1 (MF1), phyllosilicate-bearing unit (PhU), hematite ridge (HR), spectral-sloped unit (SS), layered sulfate (LS)) all fall within a similar albedo and thermal inertia range but are distinguished from one another in orbital data by distinctive combinations of secondary minerals and textures. These nine units are described in detail in the subsequent sections in order from oldest to youngest, and their characteristics are summarized in Table 2. Areas that did not fit within the defining characteristics of these nine groups, in part due to their small areal size or partial cover by sands, are left unmapped in this work.

4.1. Murray Formation Units (MF1, MF2, and MF3)

The Murray formation as originally defined in *Grotzinger et al*. [2015] is the basal part of the Mount Sharp group and has been locally studied along the route traveled by Curiosity (Figure 1e). The formation's lowest exposure is defined by a contact with the Bradbury group that is expressed as a well-defined scarp in the northeast [*Grotzinger et al*., 2015] and a more gradational, topographic rise in the southwest as mapped here. Higher in elevation, the Murray formation transitions to PhU, although this contact is obscured in several locations by HR to the northeast and the HTI1 to the southwest (Figure 5).

The Murray formation is heterogeneous in thermophysical, textural, and spectral properties (Figures 2–4 and Table 2), and these heterogeneities lead us to separate the Murray formation into three different orbitally defined units. The first unit, Murray formation 1 (MF1), has an average TI of $360 \pm 31\ J\,m^{-2}\,K^{-1}\,s^{-1/2}$ and CRISM I/F albedo integrated from 0.4–2.5 μm of 0.25 ± 0.09. HiRISE color data show that ridges and fractured bedrock characterize this unit and that it contains very few craters (Figure 4a). This is the only Murray formation unit Curiosity has explored at the time of writing.

The second unit, Murray formation 2 (MF2), has average TI clustered around $320 \pm 32\ J\,m^{-2}\,K^{-1}\,s^{-1/2}$ and CRISM I/F albedo integrated from 0.4 to 2.5 μm of 0.20 ± 0.02. This unit is heavily fractured and characterized by many sand-filled hollows and layered, blocky bedrock (Figures 4b and 4c).

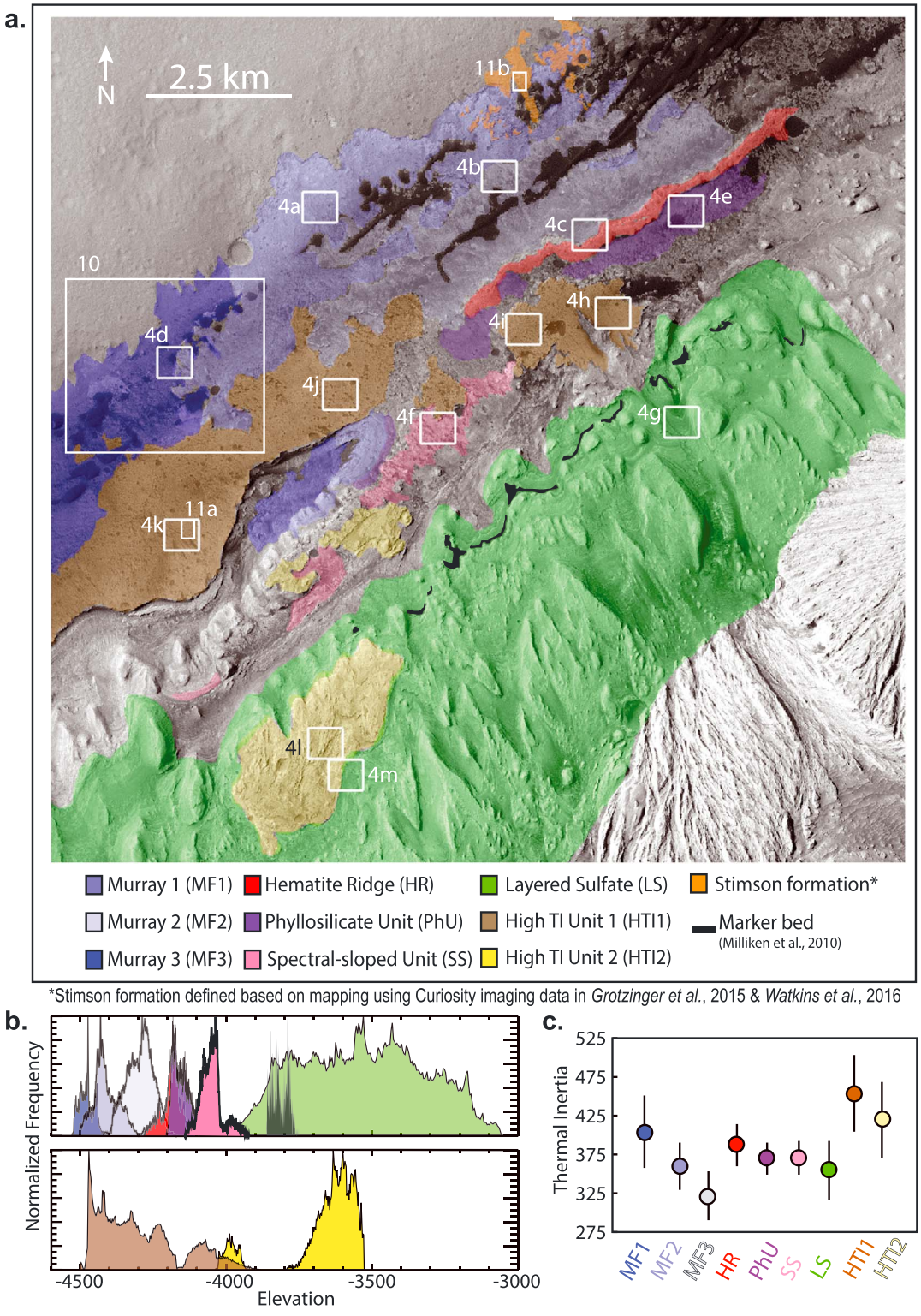

Figure 3. (a) Major Mount Sharp units defined in this study. Boxes indicate locations for detailed textures shown in Figure 4. (b) Pixels within each unit as a function of elevation. Maximum histogram values have been normalized to 1 for ease of comparison between units. (c) Average thermal inertia of each unit. Error bars show one standard deviation for pixels within unit.

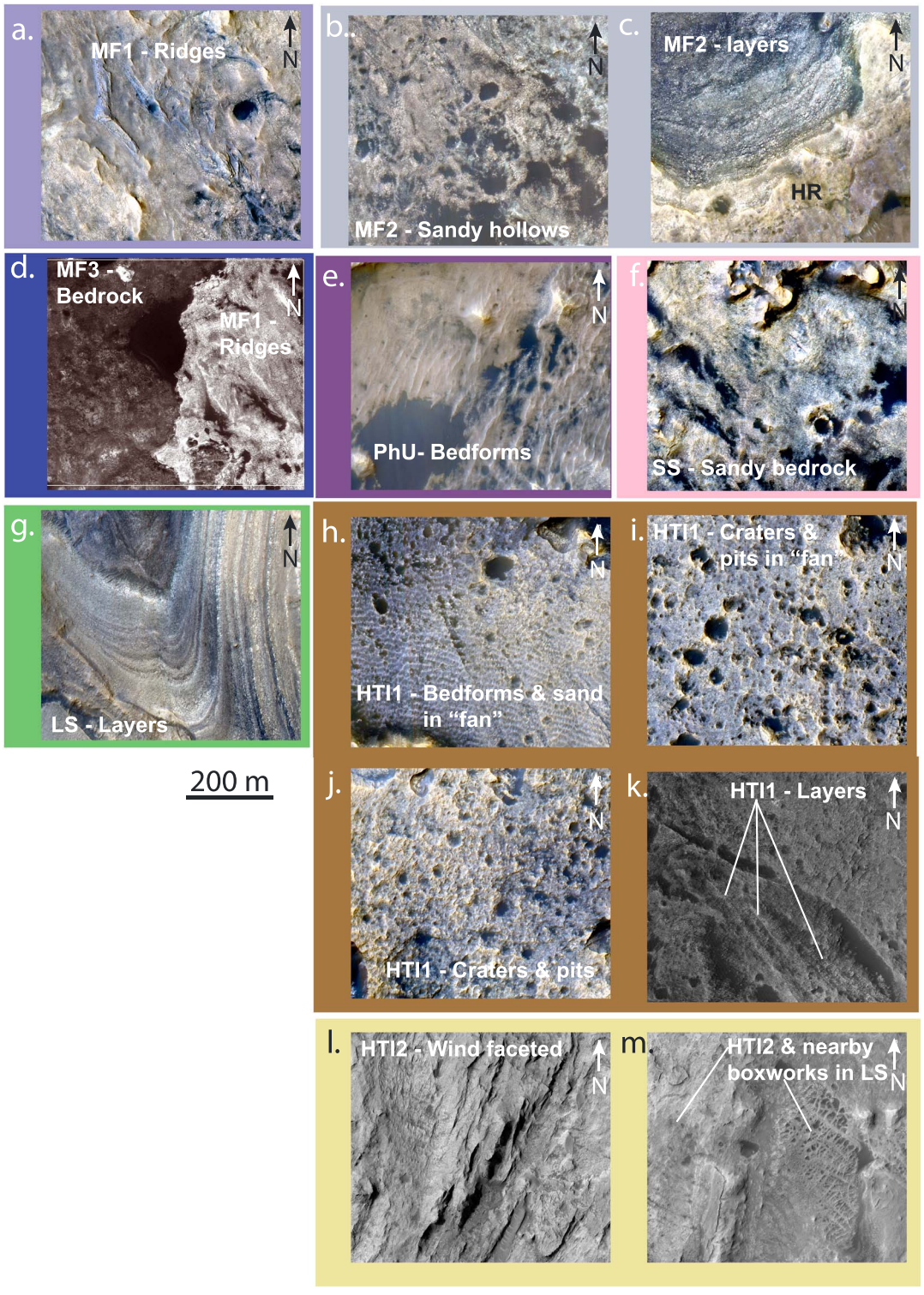

Figure 4. (a–m) HiRISE images (color where available) showing representative textures within each unit.

The third unit, Murray formation 3 (MF3), is the darkest and has an average CRISM-derived integrated Lambert albedo of 0.19 ± 0.02. This unit has a TI of $403 \pm 44\ \mathrm{J\,m^{-2}\,K^{-1}\,s^{-1/2}}$, which is the highest TI of any of the lower mound units except HTI1 and HTI2. Texturally, MF3 has few craters, blocky light-toned bedrock exposures, and decameter-scale veins and fracture fills (Figure 4d). While some of the variations in TI and

Journal of Geophysical Research: Planets

10.1002/2016JE005095

Table 2. Unit Characteristics and Relationship to Rover Mapped Units

	Rover Data [a,b]		Orbital Data				
	Formation	Unit	Abbr.	CRISM Albedo [c]	TI [c,d]	Secondary Minerals	Textures
Siccar Point group	Unnamed formation	High thermal inertia unit 2	HTI2	0.25 ± 0.02	422 ± 47	N/A	Wind-faceted ridges
	Stimson formation?	High thermal inertia unit 1	HTI1	0.20 ± 0.01	460 ± 43	N/A	Craters and pits, cemented bed forms well-defined layers, light-toned fracture, and erosion resistant polygonal fractures
Lower Mount. Sharp group	Unnamed formation	Layered sulfate	LS	0.25 ± 0.05	355 ± 38	Monohydrated and polyhydrated sulfates	Well-defined layers
	Murray formation?	Spectrally sloped unit	SS	0.22 ± 0.02	375 ± 22	Uncertain but likely iron-bearing phase	Sand-covered, crater-retaining bedrock
		Hematite ridge unit	HR	0.23 ± 0.02	395 ± 23	Hematite	More erosion resistant than surrounding terrain, crater-retaining bedrock
		Phyllosilicate unit	PhU	0.21 ± 0.01	368 ± 18	Phyllosilicates	Few fractures, reticulate texture
	Murray formation	Murray formation 2	MF2	0.20 ± 0.02	320 ± 32	Hematite, sulfates?, phyllosilicate?	Heavily fractured many sand-filled hollows, layered, and blocky bedrock
		Murray formation 1	MF1	0.25 ± 0.09	360 ± 31	Hematite, hydrated silica, phyllosilicates, and sulfates	Erosion resistant buttes and mesas contain very few craters
		Murray formation 3	MF3	0.19 ± 0.02	403 ± 44	Hematite, hydrated silica, and phyllosilicates	Few craters, blocky light-toned bedrock exposures, decameter-scale veins, and fracture fills

[a]Reflects rover progress through sol 1300.
[b]*Grotzinger et al*. [2015] and *Watkins et al*. [2016].
[c]Average value ± 1 standard deviation.
[d]$J\,m^{-2}\,K^{-1}\,s^{-1/2}$.

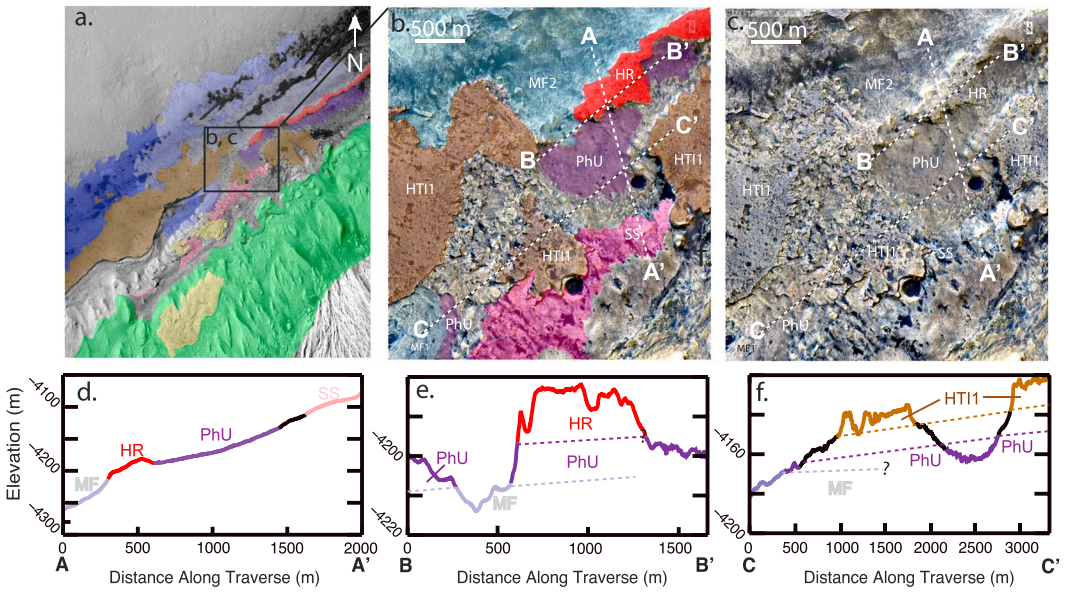

Figure 5. Transects demonstrating stratigraphic relationships. (a) Large-scale context image, (b) units and transects, (c) HiRISE color and transects, (d) transect from A-A' showing relationship between Murray formation (MF), phyllosilicate unit (PhU), hematite ridge (HR), and spectral-sloped unit (SS), (e) transect from B-B' showing relationship between MF, PhU, and HR, and (f) transect from C-C' showing relationships between MF, PhU, and high thermal inertia unit 1 (HTI1).

albedo across Murray are likely related to regolith/dust cover, the associations of these three subunits with distinct textural and spectral changes suggest differences in TI also reflect differences in cementation or grain size [*Piqueux and Christensen*, 2009].

CRISM spectral data show diverse secondary phases present in each of the three of the Murray formation units and include iron oxides, sulfates, hydrated silica, and phyllosilicates (Figures 6–8). These phases are distributed nonuniformly throughout all three of these units, as described in detail below. The assemblage of secondary phases detected by CRISM is consistent with materials already observed by the CheMin X-ray diffraction instrument on Curiosity at different locations within MF1 [*Cavanagh et al.*, 2015; *Rampe et al.*, 2016].

4.1.1. Iron Oxides

Iron oxides have four characteristic absorptions in the visible/near-infrared portion of the spectrum caused by electronic absorptions (crystal field transitions and charge transfers). The exact positions of these absorptions vary between oxide phases due to differences in the crystal structures but typically occur between 0.4–0.41 μm ($^4A_1 \leftarrow {}^6A_1$), 0.49–0.56 μm (electron pair transition, EPT), 0.65–0.71 μm ($^4T_2 \leftarrow {}^6A_1$), and 0.848–0.906 μm ($^4T_1 \leftarrow {}^6A_1$) [*Cornell and Schwertmann*, 2003]. Hematite can easily be distinguished from other iron oxides because the EPT absorption occurs at a slightly longer wavelength than other phases (~0.53 μm versus ~0.5 μm) and the $^4T_1 \leftarrow {}^6A_1$ absorption occurs at a slightly shorter wavelength (~0.86 μm versus ~0.92 μm) [*Scheinost et al.*, 1998]. Mixing of multiple iron oxides with hematite is highly nonlinear; only ~5–10 wt % of hematite mixed with other iron oxides will cause the EPT and $^4T_1 \leftarrow {}^6A_1$ absorptions to shift toward hematite-specific wavelengths, effectively masking evidence that any other iron oxides may be present [*Morris*, 1998]. Particle size and shape also have a strong effect on the spectral signature, and hematite's distinctive 0.86 μm absorption becomes less apparent or disappears completely at large (>~5 μm) and small grain sizes (<5–10 nm), often referred to as "nanophase" [*Morris et al.*, 1985].

We used ATO CRISM cubes to refine the location of iron oxide deposits at 12 m/pixel scale using end-member similarity mapping and standard CRISM parameter mapping techniques (Figures 6 and 9). Two areas within MF1 are associated with a large number of spatially coherent CRISM pixels that all have absorptions centered at 0.53 μm and 0.86 μm and also have local maxima at 0.75 μm, indicating the presence of crystalline hematite (Figures 6, 8, and 9). The first Murray hematite deposit (MH1) is situated ~4 km to the west of the hematite ridge (HR, *see section* 4.3) and is ~250 m lower in elevation. Unlike HR, hematite spectral signatures within the MH1 unit also contain a 1.9 μm H_2O combination absorption feature. Similar to HR, the hematite in MH1 is

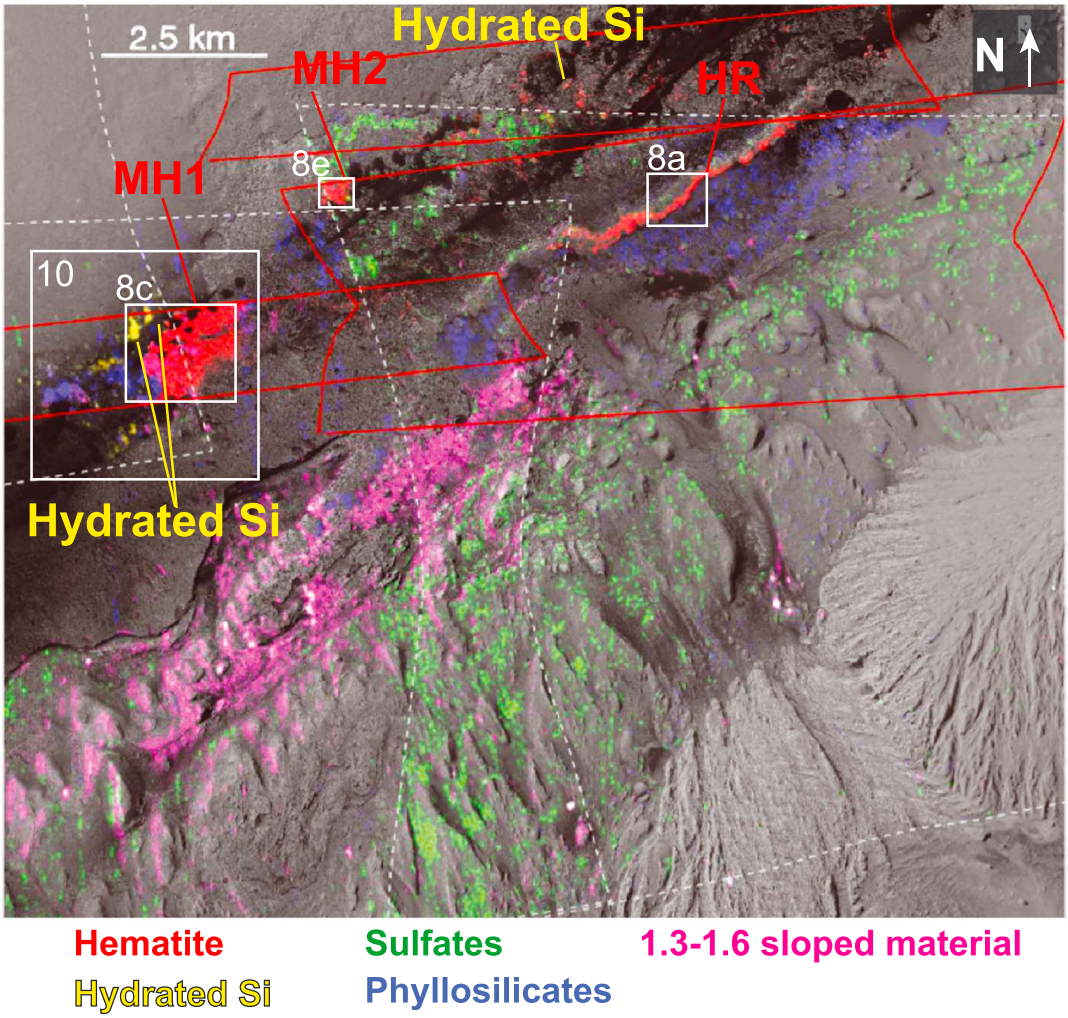

Figure 6. Secondary phases mapped in Mount Sharp using ATO parameter mapping (hematite) and end-member similarity mapping (all other phases). Coverage of CRISM ATO scenes is indicated by solid red lines, and CRISM FRT scenes are indicated by dotted gray lines. Solid white boxes indicate Figures 8 and 9 context.

stratigraphically confined. This geometry is evidenced by a sharp contact that occurs between hematite-rich and hematite-poor outcrops along a primary bedding plane that is traceable for tens of meters (Figure 9). The hematite-rich layer(s) is likely thin, indicated by the fact that the hematite spectral signature is not associated with rocks in the wall of a high standing butte that is preserved by a cap of erosion resistant HTI1 material (Figures 9b–9d). Hematite signatures do occur over a series of approximately parallel, erosion resistant fins that stand ~1–3 m tall (Figure 8c), although the fins are only a few meters in width and their compositions are not resolvable even in CRISM ATO data.

The second Murray hematite deposit (MH2) occurs at a similar elevation as MH1. This deposit shares some textural similarities with MH1, particularly an association with ridged terrain that may be filled fractures (Figures 9e and 9f). CRISM pixels within MH2 also contain a 1.9 μm H_2O combination absorption feature. Unlike MH1 and HR, there is no obvious evidence the 0.86 μm hematite-absorption spectral signature is geometrically concordant with bedding, although MH2 does occur at a local topographic high in an area that does not have well-defined bedding from orbit.

Additional isolated pixels having absorptions at 0.86 μm are also scattered throughout the Murray formation (Figure 6). These pixels have shallower 0.86 μm band depths than spectra collected from within MH1 and MH2, and these shallower band depths are due to lower hematite abundance, differences in grain size or crystallinity, or more dust cover. Several of these orbital hematite detections are adjacent to Curiosity's

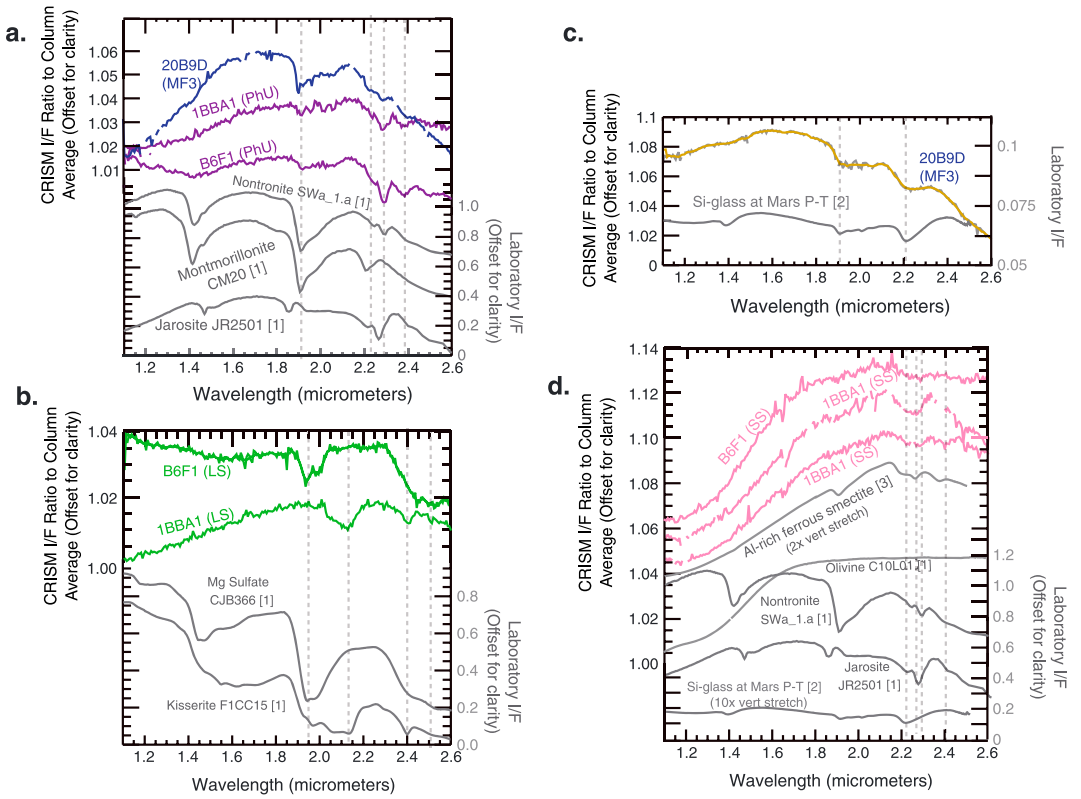

Figure 7. Representative CRISM and associated laboratory spectra. Colored spectra are from CRISM data, labeled with their originating CRISM cube and mapped unit abbreviation. Laboratory spectra sources are [1] U.S. Geological Survey (USGS) spectral library spectra [*Clark et al.*, 1993], [2] silicate glass collected under Mars temperature and pressure conditions [*Swayze et al.*, 2007], and [3] Al-rich ferrous smectite (sample E) observed under desiccating, low-O_2 conditions [*Chemtob et al.*, 2015]. (a) Phyllosilicates (b) Sulfates (c) Hydrated silica (d) Spectral slopped material.

traverse, and they begin to appear just a few meters south of locations where Curiosity has observed hematite-rich bedrock with reflectance spectral methods [*Johnson et al.*, 2016; *Wellington et al.*, 2015].

4.1.2. Hydrated Silica

Curiosity has detected outcrops in MF1 with elevated SiO_2 content [*Frydenvang et al.*, 2016] and has identified several distinct silica phases, including opal-A, cristobalite, and tridymite [*Morris et al.*, 2016]. In the visible to short wave infrared spectral range, hydrated silica phases have a pair of absorptions near 2.21 μm and 2.26 μm due to Si-OH. They also have absorptions near 1.9 μm due to H_2O and can have absorptions near 1.4 μm from an H_2O combination band and OH overtones [e.g., *Rice et al.*, 2013, and references therein].

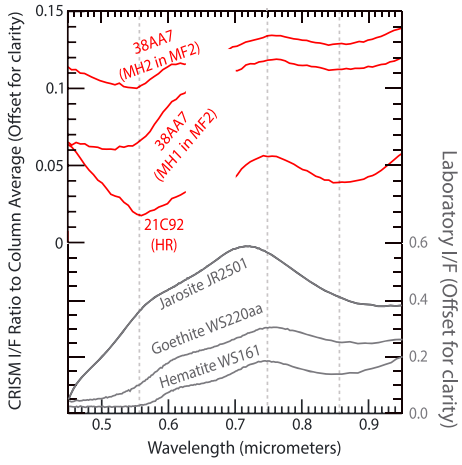

Figure 8. Spectra from massive hematite deposits compared with USGS laboratory spectra [*Clark et al.*, 1993].

CRISM ATO data show ~six contiguous pixels with a 1.9 μm absorption and broad 2.21 μm absorption, consistent with hydrated silica near the base of an active sand dune in MF1 (Figures 6 and 7c). There are no obvious morphologic features or significant HiRISE color differences associated with this ~0.01 sq km area, and we hypothesize it may represent a silica-rich portion of the Murray

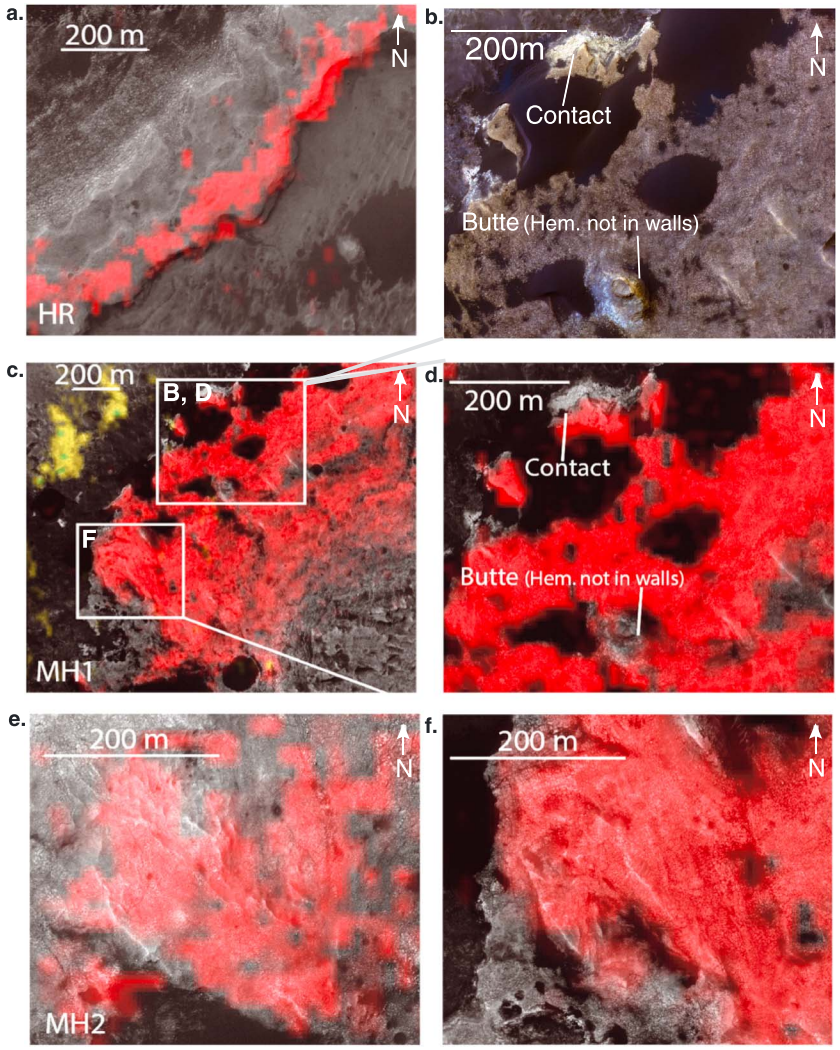

Figure 9. CRISM BD 860 parameter maps generated from regularized ATO data (red) shown atop HiRISE grayscale images indicating hematite locations. (a) Hematite ridge (HR), (b) color HiRISE from Murray hematite 1 (MH1) showing sharp contact between hematite and underlying layers, location indicated in Figure 9c, (c) MH1, (d) same area as Figure 9b showing corresponding CRISM BD860 parameter overlay in red, (e) ridged textures in Murray hematite 2 (MH2), and (f) zoom of MH1 showing area with similar ridged textures at MH2 at same scale as Figure 9e.

bedrock that is detectable in orbital data because the outcrop has been cleared of obscuring dust by recent dune migration [*Silvestro et al*., 2013].

Two isolated and spatially expansive hydrated silica deposits associated with light-toned fractures are also visible. The first deposit is located near the Bradbury-lower Mount Sharp group contact, although the exact relationship between this outcrop and the Murray formation is unclear because the nearby Bradbury-lower Mount Sharp contact is obscured by nearby dune cover [*Seelos et al*., 2014]. Deposits of hydrated silica are also discovered exposed in the walls of an eroding scarp in MF3 near the vicinity of MH1 (Figures 6 and 10c). These ~150 × 300 m^2 detections in MF3 have similar textures and fracture sizes as the detections reported several kilometers to the northeast in *Seelos et al*. [2014]. There also are scattered silica signatures near the large deposits, which correspond to low-lying bedrock and veins (Figures 10e and 10f). The veined area within MF3 is characterized by high TI and strong 1.9 μm absorption throughout.

Finally, averages of hundreds of pixels within the MF1 and MF2 formations have a 2.2 μm absorption consistent with the presence of hydrated phases, possibly including hydrated silica, through much of the Murray formation [*Milliken et al*., 2010].

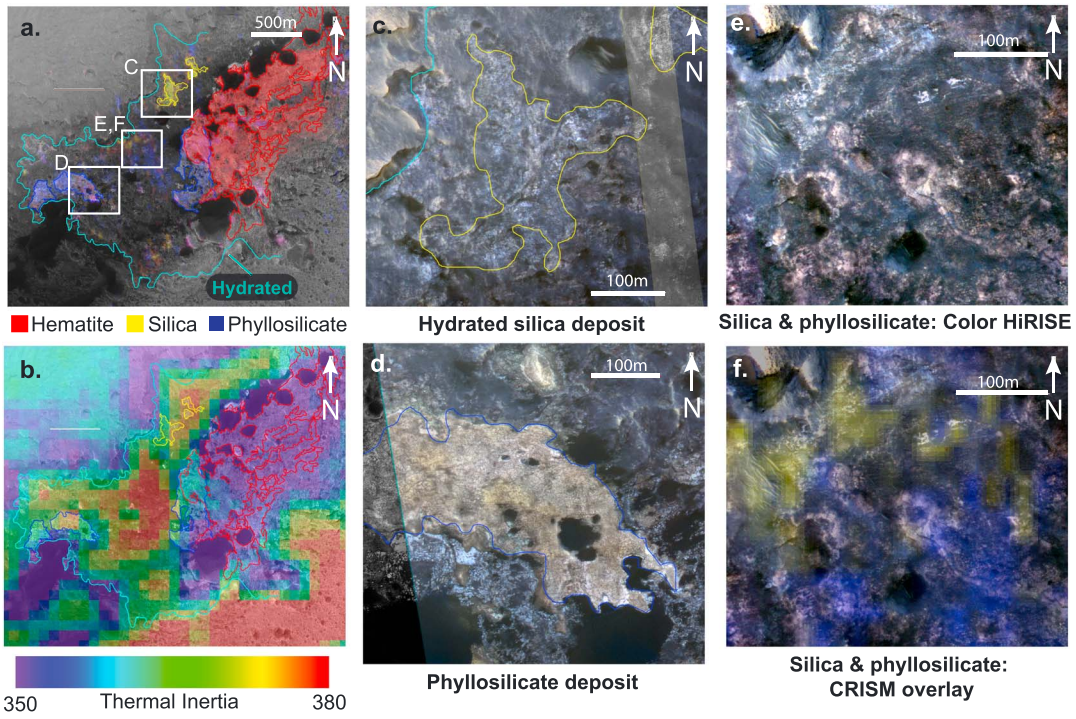

Figure 10. MF3. (a) Context view showing relationship between hematite detections (red, CRISM BD 860 parameter from ATO data), hydrated silica (yellow, BD 2200), and phyllosilicates (violet, BD 2300). Cyan outline indicates broad region containing spectra that all show evidence for hydration (BD 1900). (b) Hydrated area has increased TI compared with surrounding. (c) Color HiRISE of hydrated silica (yellow outline) present in fractures exposed in walls of eroded scarp. (d) Color HiRISE of large phyllosilicate deposit (blue outline). (e) Color HiRISE of region with intermixed hydrated silica and phyllosilicate. (f) Associated CRISM parameter overlay (yellow = silica, violet = phyllosilicate).

4.1.3. Phyllosilicates

Fe, Mg, and Al-bearing phyllosilicate phases have absorptions at 1.9 μm caused by interlayer H_2O and at ~2.2–2.3 μm due to a metal-OH stretch of the octahedral cations. The exact position of metal-OH absorption is dependent on composition, with Al-rich phyllosilicates having bands near 2.21 μm due to an Al-OH combination absorption or 2.23–2.25 due to Al,Fe-OH combination absorptions, and Fe/Mg-rich phyllosilicates having an absorption near 2.3 μm, resulting from Fe-OH and Mg-OH bends and stretches [e.g., *Bishop et al.*, 2002, and references therein]. Additional combination tones near 1.4 μm and 2.4 μm are sometimes also present.

Spatially coherent Al/Fe phyllosilicate signatures are visible in MF3 as deposits beneath MH1 and also in a nearby local topographic low to the west (Figures 6, 7a, and 10d). These deposits are ~400 m × ~700 m and characterized by fractured bedrock that is brighter than the surrounding material. The western deposit is ~70 m lower in elevation than the eastern deposit. Al/Fe phyllosilicates are also sporadically associated with light-toned material and intermingled with hydrated silica detections (Figures 10e and 10f). The MF3 phyllosilicate spectral signatures are similar to the spectral signatures of phyllosilicates higher up on Mount Sharp in the phyllosilicate unit (PhU) because they have similar absorptions near 2.2 μm and 2.3 μm indicating they are likely Fe/Mg phyllosilicates with some Al substitution [*Bishop et al.*, 2002; *Milliken et al.*, 2010] (Figure 7a). Phyllosilicate signatures are also scattered intermittently within MF1 and MF2 and reported in MF1 in *Carter and Gondet* [2016].

4.1.4. Sulfates

Hydrated sulfates can be identified in the visible to near-infrared spectral range by absorption features near 2.4 μm caused by overtones of SO_4^{2-} stretching associated with H_2O or OH [*Cloutis et al.*, 2006]. Polyhydrated sulfates also have additional absorptions near 1.9 μm due to H_2O or OH, and monohydrated sulfates have absorptions near 2.1 μm due to H_2O vibrational combinations, with the exact minimum of this position varying by cation [*Cloutis et al.*, 2006].

Spectral signatures consistent with both polyhydrated and monohydrated sulfates are present sporadically throughout MF1 and MF2 (Figures 6 and 7b). These signatures do not appear to be correlated with any obvious morphologic feature in the HiRISE data set or particular TI properties and are not spatially paired with any other secondary phases observed in CRISM data.

4.2. Phyllosilicate Unit (PhU)

The phyllosilicate unit (PhU) sits directly atop the Murray formation and is named after its strong association with a phyllosilicate CRISM spectral signature (Figures 3 and 6). This unit is identified as the "phyllosilicate trough" in *Anderson and Bell* [2010] and the "phyllosilicate layers" in *Milliken et al*. [2010]. On average PhU is higher in elevation than HR (Figure 3), but a close examination of the contact between the three units shows PhU is actually stratigraphically below the HR and above MF2 (Figure 5). This complication is an effect of northward dips of layers in the area that average ~7° ± 2.5° [*Fraeman et al*., 2013] and differential erosion.

The spectral signatures of phyllosilicates in PhU have metal-OH absorptions at ~2.2 μm and 2.3 μm, similar to the phyllosilicate signatures observed in MF3 and consistent with an Fe/Mg phyllosilicate with some Al substitution, or possibly a mixture of Al and Fe/Mg-bearing phyllosilicates. Phyllosilicates may be present as cement or authigenic phase in aeolian sandstones or be detrital grains sourced from thin beds overlying the dunes, and this relationship cannot be resolved from orbital CRISM and HiRISE data.

PhU has an average TI of $368 \pm 18\,J\,m^{-2}\,K^{-1}\,s^{-1/2}$ and CRISM I/F albedo integrated from 0.4 to 2.5 μm of 0.21 ± 0.01. This unit is distinguishable from the Murray formation and the overlying units because it is less fractured and has a distinctive reticulate texture (Figures 4e and 5), which has been hypothesized to result from partially eroded aeolian dune strata [*Milliken et al*., 2014]. The first high thermal inertia unit (HTI1) covers PhU to the southwest, and portions of PhU identified by their unique morphology and association with phyllosilicate spectral signature are visible underneath both edges of this contact (Figure 5).

4.3. Hematite Ridge (HR)

The hematite ridge (HR) unit sits on top of PhU, although the average elevation of this unit is the same and lower than PhU due to the ~7° ± 2.5° northward dip of Mount Sharp group strata at this location (Figure 3) [*Fraeman et al*., 2013]. HR has an average TI of $395 \pm 23\,J\,m^{-2}\,K^{-1}\,s^{-1/2}$ and average CRISM-integrated I/F value of 0.23 ± 0.02 and is more erosion resistant than surrounding terrain evidenced by the fact that it stands ~10 m above PhU (Figure 5). The ridge top also retains craters better than surrounding MF and PhU units (Figure 4c). HR is ~200 m wide and extends for ~6.5 km in the northeast-southwest direction. The ridge transitions to an escarpment overlain by HTI1 to the west and is obscured by surficial deposits to the east. HR is composed of well-layered materials that are geometrically concordant with overlying and underlying Mount Sharp bedding planes (Figure 4c), and CRISM data show the uppermost layer of this unit is associated with an anhydrous, hematite spectral signature [*Fraeman et al*., 2013](Figures 8 and 9).

4.4. Spectral-Sloped (SS) Unit

The spectral-sloped (SS) unit is defined primarily by its association with CRISM spectral signatures that have slopes between 1.0 and 1.6 μm which are steeper than spectral signatures from all other material in the lower mound (Figures 6 and 7d). This unit is bluer than the surrounding terrain in HiRISE false-color mosaic (Figures 4f and 5) and is characterized by sand-covered, crater-retaining bedrock. The unique spectral signature associated with this unit is likely carried by the underlying bedrock rather than overlying sand because sands concentrated in nearby depressions do not show a similar steep spectral slope. The SS unit has an average TI of $375 \pm 22\,J\,m^{-2}\,K^{-1}\,s^{-1/2}$ and integrated I/F albedo of 0.22 ± 0.02, which is comparable to the surrounding PhU and HR units. It is covered in the northeast by HTI1.

Assigning a unique material as the cause of the spectral slope is difficult; some spectra in this unit occasionally also have very weak 1.9 μm and 2.3 μm absorptions, some have broad absorptions centered near 2.25 μm, and many are featureless beyond the characteristic steep spectral slope to the level of CRISM instrument noise (Figure 7d). Possible responsible phases could include primary ferrous mafic minerals, such as olivine, that have deep absorptions near 1 μm caused by Fe^{2+} electronic transitions [*Clark*, 1999], or they could be secondary ferric phases, like iron sulfates, that sometimes have steep spectral slopes from 0.8 to 1.6 μm due to deep, Fe^{3+} spin-forbidden absorption bands [*Cloutis et al*., 2006]. In particular, jarosite also has an absorption near 2.26 μm, which if combined with a 2.2 μm absorption from hydrated silica, may explain the broad ~2.25 μm

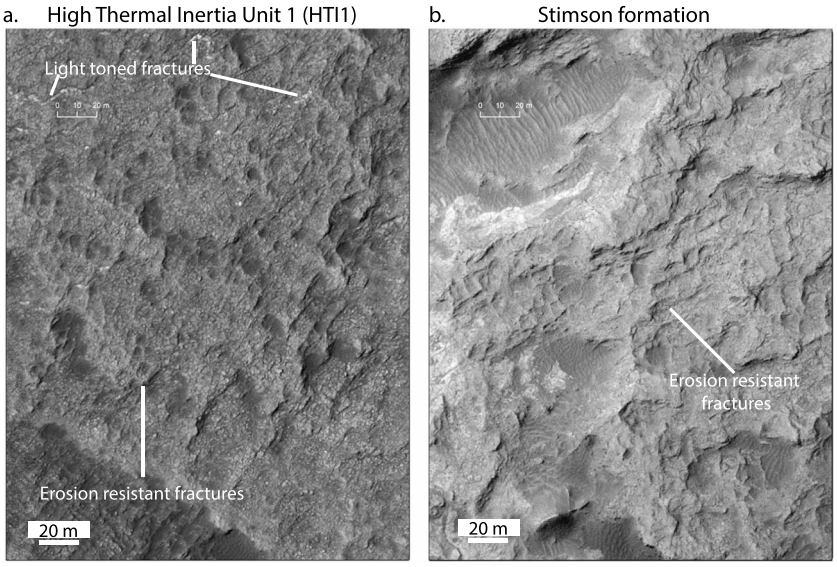

Figure 11. Polygonal, erosion resistant fractures in (a) HTI1 and (b) Stimson formation as mapped using orbital and Curiosity imaging data in *Grotzinger et al*. [2015] and *Watkins et al*. [2016].

feature seen in many spectra from this unit. Spectra from this unit, however, do not have a strong absorption at 0.9 μm, which would be expected for jarosite. Fe^{2+}-bearing phyllosilicates are also characterized by steep spectral slopes from 1 to 1.6 μm [*Chemtob et al*., 2015] and could be consistent with the weak ~1.9 μm and ~2.3 μm absorptions observed in some of the spectra [*Horgan et al*., 2015]. The lack of strong 1.9 μm H_2O absorptions, prevalent in other Mount Sharp units, correlated with the strongest ~2.25 μm phases may also implicate an anhydrous phase.

4.5. Layered Sulfate (LS)

The layered sulfate unit is characterized by its uniform-layered texture and association with spectral signatures of monohydrated and polyhydrated Mg sulfates as first reported in *Milliken et al*., 2010 (Figures 6 and 7b). The sulfate unit has an averaged CRISM-integrated I/F albedo of 0.25 ± 0.05 and average TI of 355 ± 38 J m^{-2} K^{-1} $s^{-1/2}$. Sulfate spectral signatures are strongest on exposed walls of scarps and become weaker toward the northeast portion of the unit, possibly due to cover by later materials (Figure 3). The LS unit has also been partially modified by secondary processes; fractures and boxwork structures are abundant throughout and demonstrate diagenetic fluids were likely available even toward the upper part of the lower Mount Sharp group [*Leveille et al*., 2014; *Siebach et al*., 2014].

4.6. High Thermal Inertia Units

Two units, HTI1 and HTI2, are demarcated by their high thermal inertia and distinct textures compared with the rest of NW Mount Sharp (Figures 2 and 4h–4m). CRISM data do not show any secondary phases in these units.

The first high thermal inertia unit (HTI1) has a thermal inertia of 460 ± 43 J m^{-2} K^{-1} $s^{-1/2}$ and average CRISM-integrated Lambert albedo of 0.20 ± 0.01 (Figures 2 and 3). This unit corresponds to the "draping strata" in *Grotzinger et al*. [2015]. Despite having relatively uniform thermophysical and albedo properties, HTI1 is morphologically diverse. Portions of this unit contain craters and pits (Figures 4i and 4j), cemented bed forms (Figure 4h), well-defined layers (Figure 4k), light-toned fractures (Figures 4k and 11), and erosion resistant polygonal fractures (Figures 4k and 11). There are three main large exposures of HTI1 that are visible in the study area; the western portion lies above the MF units, the central portion is located above the SS unit, and the eastern portion is at the end of a large trough and sits on top of the SS and PhU units (Figure 3).

The second high thermal inertia unit (HTI2) has an average TI of 422 ± 47 J m^{-2} K^{-1} $s^{-1/2}$ and CRISM-integrated Lambert albedo around 0.25 ± 0.02 (Figures 2, 3, and 12). Besides having a higher average albedo than HTI1, HTI2 also has a substantially different texture and is characterized by many steep, wind-faceted ridges

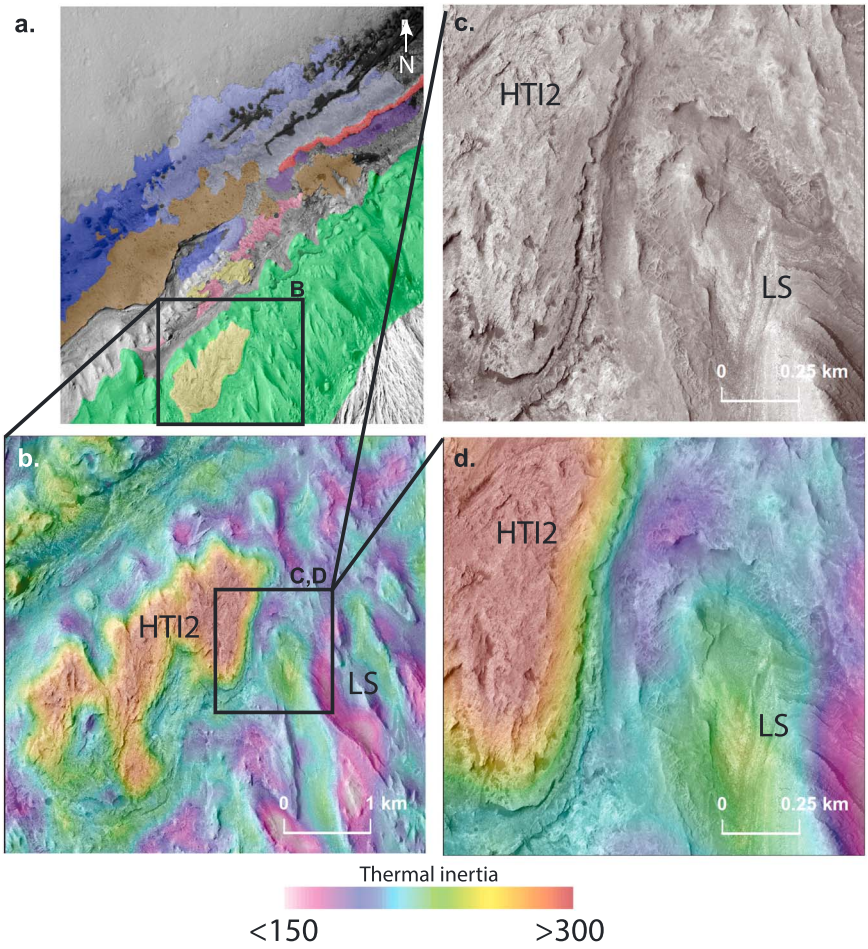

Figure 12. (a) Context image and (b–d) zoom highlighting nature of contact between HTI2 and LS. Grayscale HiRISE is shown in Figure 12c, and TI overlay is smoothed using bilinear interpolation shown in Figures 12b and 12d. The contact between HTI2 and LS is distinguished by textural and morphological changes.

(Figures 4l and 12). Many portions of HTI2 are surrounded by a highly fractured portion of the LS unit (Figure 4m) and are easily distinguished from the surrounding LS unit based on higher TI, lack of sulfate spectral signatures, and absence of well-defined layers (Figure 12).

5. Discussion

5.1. Mount Sharp Stratigraphy

Inferred stratigraphic relationships between the orbital units are summarized in Figure 13. Elevation transects generated from HiRISE DEMs show all, but the high thermal inertia units are relatively flat lying to within ~50 m over ~10 km in the exposed NW lower mound (Figure 13b). This is inline with orbital-based dip calculations of well-defined layers in SS and LS that are typically between ~3 and 6° ± 2.5° [*Milliken et al.*, 2010; *Fraeman et al.*, 2013; *Kite et al.*, 2013; *Le Deit et al.*, 2013] and confirms that the geometry of these units is consistent with a "quasi-layer cake" model. The approximately flat-lying units (MF1-3, PhU, HR, SS, and LS) are all interpreted to be members of the Mount Sharp stratigraphic group (Table 2 and Figure 13), which consists of rocks in Mount Sharp that are located below an unconformity that separates hydrated from anhydrous rocks as observed in orbital data (Figure 1) [*Milliken et al.*, 2010; *Grotzinger et al.*, 2015].

Based on the contact relationships (Figure 5) between the Mount Sharp group units and analysis of HiRISE DEM mosaic, we agree with previous authors that the units within the Murray formation (MF3, MF1, and MF2) are the oldest components of the Mount Sharp group. The phyllosilicate unit (PhU) sits directly atop MF2, then followed by the hematite ridge (HR) and/or spectrally sloped layer (SS), and finally the layered

Journal of Geophysical Research: Planets
10.1002/2016JE005095

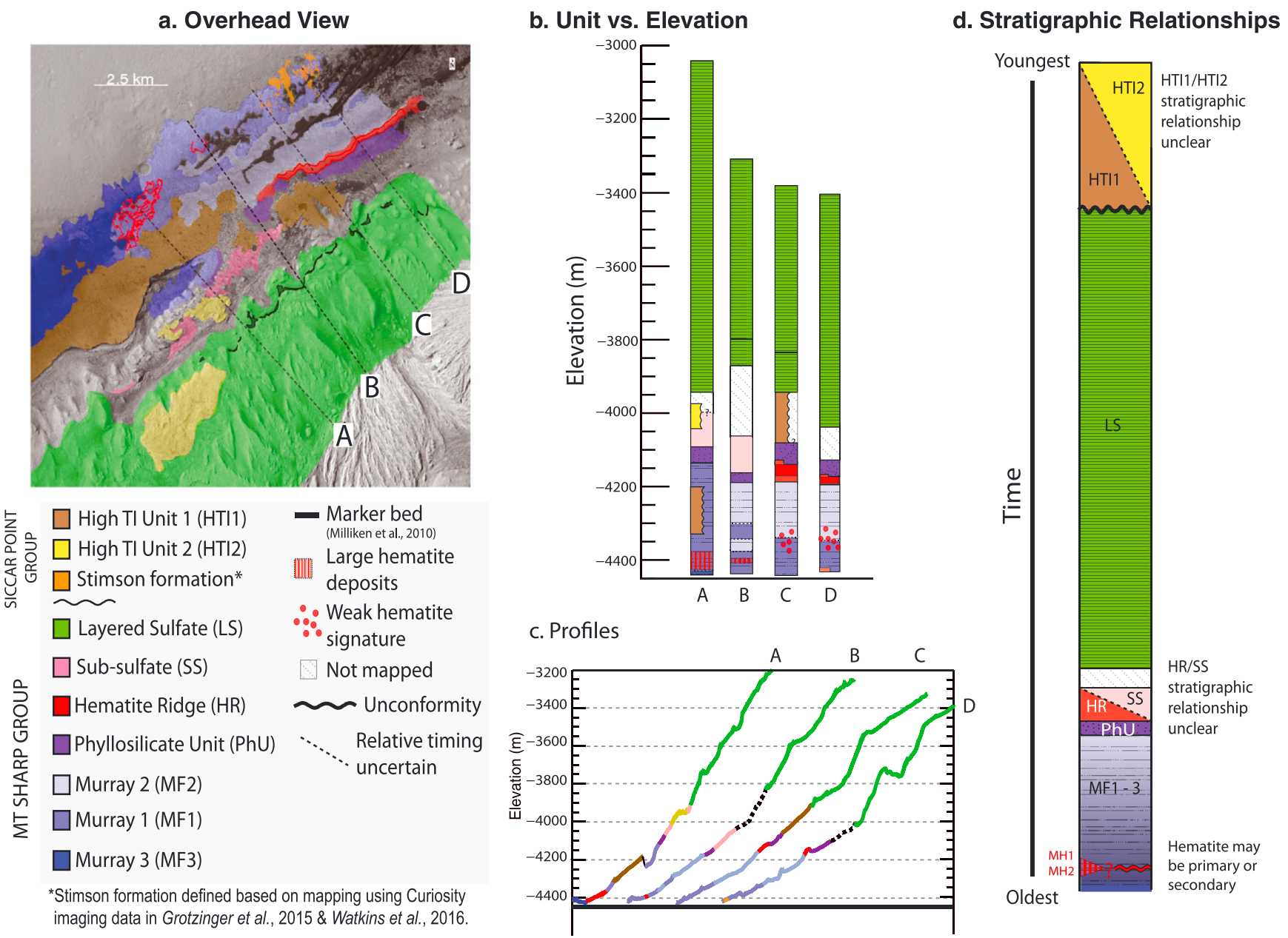

Figure 13. (a) Transects over major Mount Sharp units and (b–c) their elevation profiles. (d) Stratigraphic relationships between orbital defined units in this study.

sulfates (LS). The stratigraphic relationship between HR and SS is unclear because there are no visible contacts between these two units, and uncertainties associated with orbital-based dip measurements of the layers within HR and SS preclude a definitive statement about which unit projects above or below the other.

The two high thermal inertia units (HTI1 and HTI2) span a wide range of elevations compared with primary Mount Sharp units (Figure 3c) and are, therefore, interpreted to unconformably overlie the Mount Sharp group units. Transects across these units also show they are topographically above primary Mount Sharp group units (Figure 11c). The conclusions are similar to conclusions about some portions of these units that were noted in previous mapping studies [*Anderson and Bell*, 2010; *Milliken et al*., 2014; *Grotzinger et al*., 2015]. We categorize these units as members of a newly defined Siccar Point group, named after a promontory in a fan-shaped portion of the deposit (exact location to be determined as Curiosity moves closer to the area), and defined as a stratigraphic group that unconformably overlies the Mount Sharp group (Figure 13). The timing of the formation of HTI2 with respect to HTI1 is uncertain, but both are inferred to be younger than the LS unit based on superposition relationships (Figure 13).

Based on the similarities in thermophysical, spectral, and some morphologic features in the sections of HTI1, we hypothesize this unit was originally contiguous and emplaced sometime after deposition and initial erosion of the Mount Sharp group units. More erosion occurred after HTI1 was deposited, leaving only the more resistant portions behind. Veins and erosion resistant fractures visible in portions of HTI1 (Figure 11) indicate diagenetic rock-water interactions occurred within this unit, which may have led to differential cementation that preferentially hardened the portions that remain today. Some late-stage cementing fluids may have been channeled through the large geomorphic trough located to upslope of the easternmost portion of HTI1, explaining the fan-like shape of this easternmost section.

We hypothesize a depositional scenario for HTI1 similar to aeolian depositional scenarios proposed for the Stimson formation. Curiosity data have shown the Stimson formation is comprised of cross-bedded aeolian sandstones that infill and onlap the dissected Murray formation [*Grotzinger et al*., 2015; *Banham et al*., 2016; *Watkins et al*., 2016]. Morphologic and spectral similarities between other portions of HTI1 and the Stimson formation (Figure 11), as well as the similarly high thermal inertia of both units compared with surrounding Mount Sharp material are suggestive that the Stimson formation may have similar physical properties as these high thermal inertia units. This leads us to hypothesize that HTI1 was formed by a similar process as the Stimson formation, possibly at the same time, and they may have even comprised a contiguous deposit. Curiosity can test this hypothesis by gathering information about meter-scale bedding geometries, submillimeter-scale grain size distributions, chemistry, and mineralogy of both units.

5.2. Thermophysical Variability

The Murray formation has the most variable thermophysical properties of any Mount Sharp group units (Figures 2 and 3). While some of these variations may be related to differences in sand/dust cover, the associations of distinct textural and spectral changes with changing TI suggest there may also be changes in the thermal conductivity of the bedrock of the Murray formation caused by differences in cementation and/or grain size. The lack of linear-mixing trends between dunes, MF2, and MF3 on the integrated CRISM I/F versus TI scatterplot (Figure 2) is also suggestive that something more than variability in sand cover is driving changes in TI throughout this unit. We hypothesize multiple episodes of burial and diagenesis of this unit may have caused differential compaction and cementation, and Curiosity can test this hypothesis by investigating chemical and mineralogical differences in MF1 and MF2.

The higher TI values of HTI1 and HTI2 in comparison with the Mount Sharp group units also most likely reflect differences in cementation and/or grain size. The presence of veins and raised ridges within HTI1 and within the portion of LS surrounding HTI2 demonstrates both high thermal inertia units were also exposed to diagenetic fluids at a later stage of Mount Sharp development (Figure 11). If the majority of HTI1 indeed formed by a similar set of processes as the Stimson formation, HTI1 unit may also be a sandstone, originally proposed in *Milliken et al*. [2014]. In this case, HTI1 would be coarser grained and therefore more permeable than the underlying Murray mudstone. Diagenetic fluids could preferentially travel through this unit, resulting in increased cementation and the higher TI values observed today. This hypothesis can be tested by Curiosity through mineralogical and chemical measurements integrated with micrometer scale imaging of outcrops in HTI1 and surrounding, lower TI materials.

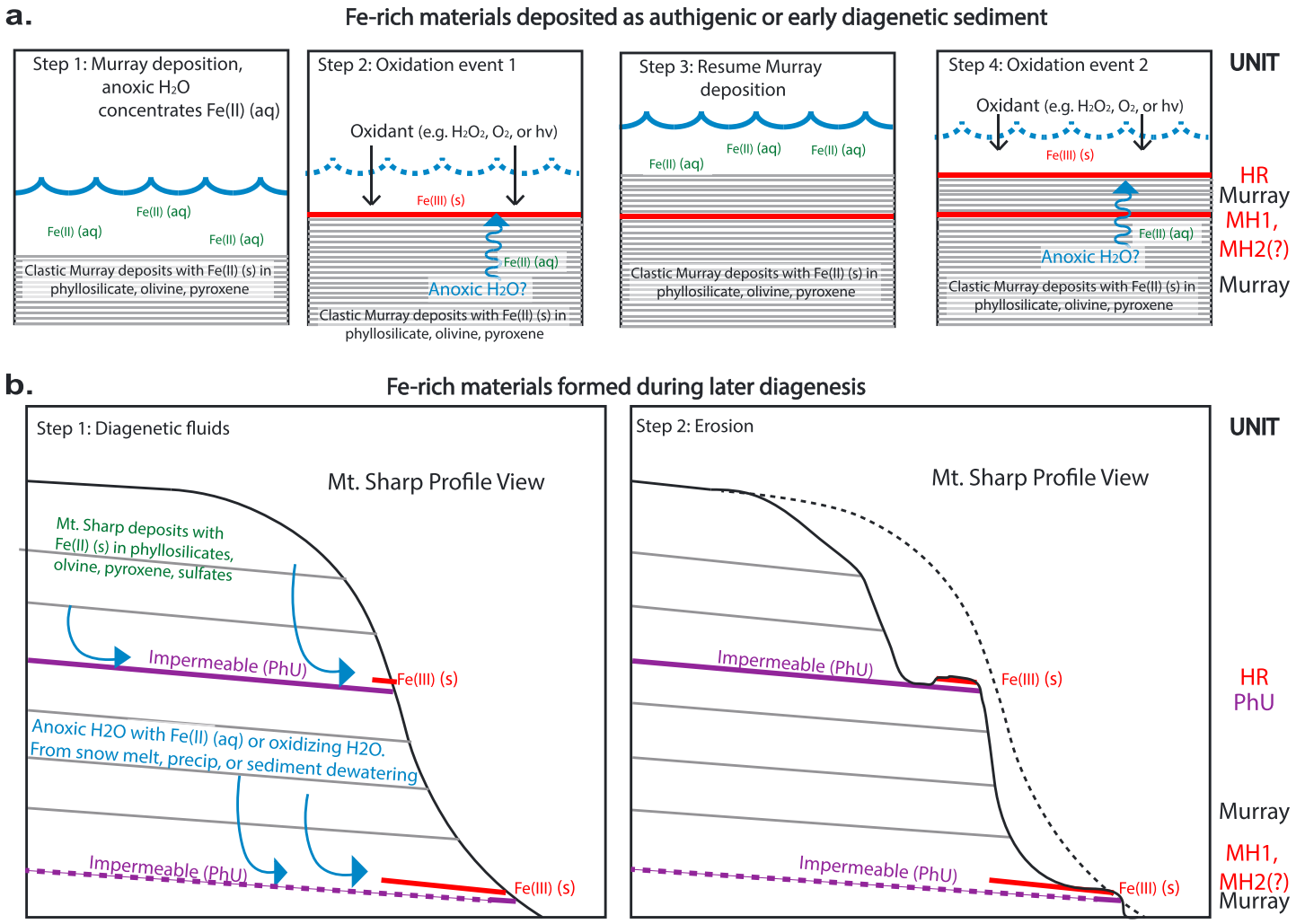

Figure 14. Cartoon schematic depicting hypothesized geologic settings to explain distribution of stratigraphically controlled hematite deposits. (a) Hematite forms concurrently with Mount Sharp through direct precipitation of Fe^{2+} at redox interfaces. (b) Hematite forms as a secondary diagenetic phase by stratigraphically controlled waters.

5.3. Spatial Distribution of Secondary Phases: Silica and Hematite

Recent Curiosity results suggest at least two episodes of silica enrichment are recorded in the Murray and Stimson formation rocks. These episodes include an initial primary silica enrichment during deposition of the Murray formation [*Morris et al.*, 2016] followed by a late-stage enrichment along fractures or permeable layers within fractures of the Murray formation and the unconformable Stimson formation [*Frydenvang et al.*, 2016; *Yen et al.*, 2016]. The hydrated silica spectral signature seen in the average Murray formation spectrum [*Milliken et al.*, 2010] and in specific outcrops visible with CRISM ATO data could be consistent with initial silica deposition, later stage enrichment, or both. The morphology of the two spatially extensive silica deposits that are associated with veins and fractures within MF3 and near the Murray formation-Bradbury group contact [*Seelos et al.*, 2014] indicates that these deposits were most likely formed in the second episode of silica enrichment that occurred after the emplacement of the Stimson formation, and the widespread nature of these deposits demonstrates that this late-stage silica enrichment was pervasive and widespread.

CRISM ATO data reveal at least two of the three large hematite deposits (MH1 and HR) in the NW quadrant of lower Mount Sharp that are closely associated with discrete stratigraphic zones that are conformable with other Mount Sharp layers. The lower boundary of MH1 is expressed as a sharp contact traceable for tens of meters with the underlying Murray formation bedrock, while the hematite in HR is confined to the uppermost

stratum of a ridge (Figure 9). Both MH1 and HR are sitting atop spectrally similar, large phyllosilicate deposits, hinting that there may be a genetic link between the two phases. The third large deposit (MH2) has no obvious morphologic boundaries to define its boarders, although it does share textural characteristics with MH1 and occurs at a similar elevation. Assuming approximately flat-lying layers would place it at the same stratigraphic position at MH1 (Figures 9 and 13).

That MH1 and HR are both closely aligned with Mount Sharp stratigraphic boundaries suggests their presence is controlled by primary facies distributions. We propose two end-member scenarios to explain the timing of hematite formation: (1) hematite (or a precursor phase that later transformed to hematite) is an authigenic phase that formed concurrently with the processes that deposited Murray formation strata or (2) hematite is a product of diagenetic fluids whose pathways were controlled by stratigraphically determined residual matrix porosity or fracture porosity (Figure 14).

5.4. Redox Conditions in Mount Sharp's History

The hematite in HR, MH1, and MH2 most likely formed at a redox interface where dissolved Fe^{2+} was oxidized and then relatively insoluble Fe^{3+} precipitated out of solution. Direct precipitation of Fe^{3+} from a low pH fluid is less likely because there is little evidence for large deposits of other secondary phases expected to form in highly acidic environments, and there is no obvious source to generate the acidity needed to maintain Fe^{3+} in solution [*Fraeman et al*., 2013]. That multiple, spatially extensive hematite deposits occur in at least two separate elevations in Mount Sharp's stratigraphy suggest redox interfaces were widespread throughout time and/or space during Mount Sharp's formation and evolution. We hypothesize two possible geologic settings for the deposition of hematite or, more likely, deposition of a precursor iron oxide that transformed to hematite over time (Figure 14).

In the first scenario (Figure 12a), Fe^{2+} is first concentrated in the lacustrine setting that is inferred to have deposited much of the Murray formation [*Grotzinger et al*., 2015]. Fe^{2+} would be sourced from surface and groundwater interaction with pyroxene, olivine, and/or secondary phyllosilicates. Oxidation events during at least two periods of lake deposition, to explain hematite deposits at two stratigraphic levels, would oxidize Fe^{2+} to an insoluble Fe^{3+} phase and lead to the precipitation of hematite, or more likely a less thermodynamically stable precursor such as ferrihydrite, goethite, or possibly schwertmannite [*Hurowitz et al*., 2010]. The source of periodic, localized oxidizing events is uncertain, but may have occurred during periods of depositional hiatus and evaporation, where lake levels were shallow enough to permit UV oxidation [e.g., *Hurowitz et al*., 2010] or periods of active volcanism that increased the amount of photochemically produced atmospheric oxidants (O_2, O_3, OH, and peroxides) [*Zolotov and Mironenko*, 2007].

An alternative scenario proposes that the iron oxides instead formed by later, diagenetic fluids that percolated along stratigraphically controlled residual matrix porosity or fracture porosity. Anoxic diagenetic fluids with dissolved Fe^{2+} ions, perhaps from nearby sulfates, mafic materials, or phyllosilicates, would precipitate ferric oxides upon mixing with oxidizing fluids migrating from other fluid source areas (Figure 12b). The abundance of boxwork structures several hundred meters above the hematite ridge demonstrates that there was water available for diagenetic transformations at even higher elevations than HR at some point in Mount Sharp's history [*Anderson and Bell*, 2010; *Andrews-Hanna et al*., 2012; *Kite et al*., 2013; *Siebach and Grotzinger*, 2014], and these fluids could have been sourced from high groundwater tables, snowmelt, or dewatering of Mount Sharp sediments due to burial. Downward infiltration of these surface waters may have caused fluid mixing with evolved basin waters at greater depths.

Analyses of the prevalence and type of iron-bearing phases by Curiosity could resolve these scenarios. In particular, the occurrence of hematite, magnetite, and iron-bearing sulfides, sulfates, and silicates will constrain the redox conditions. The nature of contact relationships with the hematite units and underlying phyllosilicates and the spectral slope unit, resolvable with rover multispectral camera and remote chemical data, may be particularly important to deciphering the time history.

6. Summary and Conclusions

We have generated a refined geologic map and stratigraphy of lower Mount Sharp using data from new spectral and morphologic products derived from three orbital instruments (CRISM, THEMIS, and HiRISE), merged within a GIS framework to allow for coordinated analyses. The Mount Sharp group consists of seven broad,

relatively flat-lying units that are delineated by differences in texture, mineralogy, and thermophysical properties.

1. The Murray formation divides into three units based on spatially coherent differences in thermophysical, textural, and spectral properties. While some of the variations in TI and albedo across Murray are likely related to regolith/dust cover, the associations of these three units with distinct textural and spectral changes suggest differences in TI also reflect differences in cementation or grain size. CRISM spectral data show a wide diversity of secondary phases including hematite, hydrated silica, sulfates, and phyllosilicates present in the Murray formation.
2. A phyllosilicate-bearing unit is distinguishable because it is less fractured and has a distinctive reticulated texture that has been hypothesized to be preserved, partially reworked dunes [*Milliken et al*., 2014]. It has an iron, aluminum-phyllosilicate spectral signature throughout the unit.
3. A hematite-capped ridge unit is composed of finely layered materials that are conformable with overlying and underlying Mount Sharp bedding planes. CRISM data show that the uppermost layer of this unit is associated with an anhydrous, hematite spectral signature [*Fraeman et al*., 2013].
4. A unit defined primarily by its association with CRISM spectral signatures has slopes between 1.0 and 1.6 μm that are steeper than spectral signatures from all other material in the lower mound, is bluer than the surrounding terrain in the HiRISE false-color mosaic, and is characterized by sand-covered, crater-retaining bedrock. The source of the strong spectral slope is unclear but is likely related to an iron-bearing phase.
5. A layered sulfate unit is characterized both by its distinctive layered texture and also by its association with scattered spectral signatures of monohydrated and polyhydrated Mg sulfates. Evidence for secondary processes such as fractures and boxwork structures are abundant throughout this unit.

The Siccar Point group unconformably overlies the Mount Sharp group and contains two units delineated by their higher thermal inertias and lack of secondary phases as well as the Stimson formation. The first high thermal inertia unit is morphologically diverse and contains craters and pits, fossilized bed forms, layers, and erosion resistant polygonal fractures. The second high thermal inertia unit is characterized by many wind-faceted ridges.

The two spatially extensive silica deposits associated with veins and fractures near the Murray formation-Bradbury group contact are most likely remnants of the later stage silica enrichment, and the widespread nature of these deposits shows this late-stage silica enrichment was pervasive and widespread. At least two laterally extensive hematitic deposits are also present at different stratigraphic intervals, and both are geometrically conformable with lower Mount Sharp strata. The hematite (or a precursor iron oxide) in these deposits either formed concurrently during deposition of the Mount Sharp group or within fluid migration pathways associated with stratigraphically controlled diagenetic overprinting. The occurrence of hematite at multiple stratigraphic horizons within the Mount Sharp sedimentary sequence suggests redox interfaces were widespread in space and/or in time. Curiosity will explore these units and be able to test hypotheses about Mount Sharp formation and evolution by complementing the orbital-based observations with fine-scale imaging, chemical, and mineralogical analyses.

Acknowledgments

We thank two anonymous reviewers for their careful reading and insight comments that improved the quality of this manuscript. Thanks to Lulu Pan for providing helpful advice on CRISM parameter mapping techniques, Ara Oshagan for assistance in generating the HiRISE color mosaic, Dawn Sumner for nomenclature guidance, and Kathryn Stack Morgan for fruitful discussions about orbital mapping interpretations and sharing her general knowledge of the Gale Crater geologic context. A.A.F. was partially supported by a W.M. Keck Institution for Space Studies Postdoctoral Fellowship and Caltech Geological and Planetary Sciences Texaco Postdoctoral Fellowship. A portion of this research was also carried out at the Jet Propulsion Laboratory, California Institute of Technology, under a contract with the National Aeronautics and Space Administration and funded through the internal Research and Technology Development program. B. L.E. was partially supported by an MSL Participating Scientist Program grant. All raw data products supporting the conclusions of this work can be obtained from the NASA Planetary Data System (PDS).

References

Anderson, R., and J. Bell (2010), Geologic mapping and characterization of Gale Crater and implications for its potential as a Mars Science Laboratory landing site, *Int. J. Mars Sci. Explor.*, *4*, 76–128, doi:10.1555/mars.2010.0004.

Andrews-Hanna, J. C., A. Soto, and M. I. Richardson (2012), The hydrologic and climatic context of the Gale crater sedimentary mound, Third Conf. on Early Mars, #7038.

Arvidson, R. E., et al. (2014a), Terrain physical properties derived from orbital data and the first 360 sols of Mars Science Laboratory Curiosity rover observations in Gale Crater, *J. Geophys. Res. Planets*, *119*, 1322–1344, doi:10.1002/2013JE004605.

Arvidson, R. E., et al. (2014b), Ancient aqueous environments at Endeavour Crater, Mars, *Science*, *343*(6169), doi:10.1126/science.1248097.

Banham, S. G., S. Gupta, D. Rubin, J. A. Watkins, D. Sumner, J. Grotzinger, K. Lewis, K. Edgett, L. Edgar, and K. Stack (2016), Reconstruction of an Ancient Eolian Dune Field at Gale Crater, Mars: Sedimentary analysis of the Stimson formation, 47th Lunar and Planetary Science Conference.

Bishop, J., E. Murad, and D. Dyar (2002), The influence of octahedral and tetrahedral cation substitution on the structure of smectites and serpentines as observed through infrared spectroscopy, *Clay Miner.*, *37*(4), 617–628.

Borlina, C. S., B. L. Ehlmann, and E. S. Kite (2015), Modeling the thermal and physical evolution of Mount Sharp's sedimentary rocks, Gale Crater, Mars: Implications for diagenesis on the MSL Curiosity rover traverse, *J. Geophys. Res. Planets*, *120*, 1396–1414, doi:10.1002/2015JE004799.

Calef, F., et al. (2013), Geologic mapping of the Mars Science Laboratory landing ellipse, 44th Lunar and Planetary Science Conference.

Carter, J., and B. Gondet (2016), MSL Homing in on a large smectite clay deposit: An orbital perspective, 47th Lunar and Planetary Science Conference.
Cavanagh, P. D., et al. (2015), Confidence Hills mineralogy and CheMin results from Base of Mt. Sharp, Pahrump Hills, Gale crater, Mars, 46th Lunar and Planetary Science Conference Houston.
Chemtob, S. M., R. N. Nickerson, R. V. Morris, D. G. Agresti, and J. Catalano (2015), Synthesis and structural characterization of ferrous trioctahedral smectites: Implications for clay mineral genesis and detectability on Mars, *J. Geophys. Res. Planets*, *120*, 1119–1140, doi:10.1002/2014JE004763.
Clark, R. N. (1999), Chapter 1: Spectroscopy of rocks and minerals, and principles of spectroscopy, in *Manual of Remote Sensing*, edited by A. N. Rencz, pp. 3–58 , John Wiley, New York.
Clark, R. N., G. A. Swayze, A. J. Gallagher, T. V. V. King, and W. M. Calvin (1993), The U. S. Geological Survey, Digital Spectral Library: Version 1: 0.2 to 3.0 microns, *U.S. Geol. Surv. Open File Rep. 93-592*, 1340 pp.
Cloutis, E., et al. (2006), Detection and discrimination of sulfate minerals using reflectance spectroscopy, *Icarus*, *184*(1), 121–157, doi:10.1016/j.icarus.2006.04.003.
Cornell, R. M., and U. Schwertmann (2003), *The Iron Oxides: Structure, Properties, Reactions, Occurrences, and Uses* 2nd, completely rev. and extended ed., xxxix, , pp. 664 , Wiley-VCH, Weinheim.
Edwards, C. S., J. L. Bandfield, P. Christensen, and R. Fergason (2009), Global distribution of bedrock exposures on Mars using THEMIS high-resolution thermal inertia, *J. Geophys. Res.*, *114*, E11001, doi:10.1029/2009JE003363.
Edwards, C. S., K. J. Nowicki, P. R. Christensen, J. Hill, N. Gorelick, and K. Murray (2011), Mosaicking of global planetary image datasets: 1. Techniques and data processing for Thermal Emission Imaging System (THEMIS) multi-spectral data, *J. Geophys. Res.*, *116*, E10008, doi:10.1029/2010JE003755.
Fergason, R., P. Christensen, M. Golombek, and T. Parker (2012), Surface properties of the Mars Science Laboratory candidate landing sites: Characterization from orbit and predictions, *Space Sci. Rev.*, *170*(1), 739–773, doi:10.1007/s11214-012-9891-3.
Fraeman, A. A., et al. (2013), A hematite-bearing layer in Gale Crater, Mars: Mapping and implications for past aqueous conditions, *Geology*, *41*(10), 1103–1106, doi:10.1130/G34613.1.
Frydenvang, J., et al. (2016), Discovery of silica-rich lacustrine and eolian sedimentary rocks in Gale Crater, Mars, 47th Lunar and Planetary Science Conference.
Golombek, M., et al. (2012), Selection of the Mars Science Laboratory landing site, *Space Sci. Rev.*, *170*(1-4), 641–737, doi:10.1007/s11214-012-9916-y.
Grotzinger, J. P., et al. (2012), Mars Science Laboratory mission and science investigation, *Space Sci. Rev.*, *170*(1-4), 5–56, doi:10.1007/s11214-012-9892-2.
Grotzinger, J. P., et al. (2015), Deposition, exhumation, and paleoclimate of an ancient lake deposit, Gale crater, Mars, *Science*, *350*(6257), doi:10.1126/science.aac7575.
Grotzinger, J., and R. Milliken (2012), The sedimentary rock record of Mars: Distribution, origins, and global stratigraphy, *Sediment. Geol. Mars*, *102*, 1–48.
Horgan, B., M. Rice, and S. Ackiss (2015), Constraints on the formation and alteration history of Mt. Sharp, Gale Crater, Mars, from a new CRISM mineral map, 46th Lunar and Planetary Science Conference.
Hurowitz, J. A., W. Fischer, N. J. Tosca, and R. E. Milliken (2010), Origin of acidic surface waters and the evolution of atmospheric chemistry on early Mars, *Nat. Geosci.*, *3*(5), 323–326, doi:10.1038/Ngeo831.
Jakosky, B. M. (1986), On the thermal properties of Martian fines, *Icarus*, *66*(1), 117–124, doi:10.1016/0019-1035(86)90011-4.
Johnson, J. R., et al. (2016), Constraints on iron sulfate and iron oxide mineralogy from ChemCam visible/near-infrared reflectance spectroscopy of Mt. Sharp basal units, Gale Crater, Mars, *Am. Mineral.*, doi:10.2138/am-2016-5553, in press.
Kieffer, H. H. (2013), Thermal model for analysis of Mars infrared mapping, *J. Geophys. Res. Planets*, *118*, 451–470, doi:10.1029/2012JE004164.
Kieffer, H. H., S. C. Chase, E. Miner, G. Münch, and G. Neugebauer (1973), Preliminary report on infrared radiometric measurements from the Mariner 9 spacecraft, *J. Geophys. Res.*, *78*(20), 4291–4312, doi:10.1029/JB078i020p04291.
Kite, E. S., K. W. Lewis, M. P. Lamb, C. E. Newman, and M. I. Richardson (2013), Growth and form of the mound in Gale Crater, Mars: Slope wind enhanced erosion and transport, *Geology*, *41*(5), 543–546, doi:10.1130/G33909.1.
Kreisch, C., R. Arvidson, J. O'Sullivan, K. Li, D. Politte, J. Finkel, E. Guinness, N. Stein, and A. Fraeman (2015), *Log-Likelihood Method of Reducing Noise in CRISM Along-Track Oversampled Hyperspectral Images*, paper presented at Computational Optical Sensing and Imaging, The Optical Society, Arlington, VA.
Kronyak, R. E., L. C. Kah, M. Nachon, N. Mangold, R. C. Weins, R. Williams, J. Schieber, and J. Grotzinger (2015), Distribution of mineralized veins from Yellowknife Bay to Mount Sharp, Gale Crater, Mars: Insight from textural and compositional variation, 46th Lunar and Planetary Science Conference.
Le Deit, L., E. Hauber, F. Fueten, M. Pondrelli, A. P. Rossi, and R. Jaumann (2013), Sequence of infilling events in Gale Crater, Mars: Results from morphology, stratigraphy, and mineralogy, *J. Geophys. Res. Planets*, *118*, 2439–2473, doi:10.1002/2012JE004322.
Leveille, R. J., et al. (2014), Chemistry of fracture-filling raised ridges in Yellowknife Bay, Gale Crater: Window into past aqueous activity and habitability on Mars, *J. Geophys. Res. Planets*, *119*, 2398–2415, doi:10.1002/2014JE004620.
Malin, M. C., and K. S. Edgett (2000), Sedimentary rocks of early Mars, *Science*, *290*(5498), 1927–1937, doi:10.1126/science.290.5498.1927.
McEwen, A. S., et al. (2007), Mars Reconnaissance Orbiter's High Resolution Imaging Science Experiment (HiRISE), *J. Geophys. Res.*, *112*, E05S02, doi:10.1029/2005JE002605.
McGuire, P. C., et al. (2009), An improvement to the volcano-scan algorithm for atmospheric correction of CRISM and OMEGA spectral data, *Planet. Space Sci.*, *57*(7), 809–815, doi:10.1016/j.pss.2009.03.007.
Milliken, R. E., J. P. Grotzinger, and B. J. Thomson (2010), Paleoclimate of Mars as captured by the stratigraphic record in Gale Crater, *Geophys. Res. Lett.*, *37*, L04201, doi:10.1029/2009GL041870.
Milliken, R. E., R. C. Ewing, W. W. Fischer, and J. Hurowitz (2014), Wind-blown sandstones cemented by sulfate and clay minerals in Gale Crater, Mars, *Geophys. Res. Lett.*, *41*, 1149–1154, doi:10.1002/2013GL059097.
Morris, R. V. (1998), Goldenrod pigments and the occurrence of hematite and possibly goethite in the Olympus-Amazonis region of Mars, *Icarus*, *134*(1), 1–10, doi:10.1006/icar.1998.5939.
Morris, R. V., H. V. Lauer, C. A. Lawson, E. K. Gibson, G. A. Nace, and C. Stewart (1985), Spectral and other physicochemical properties of submicron powders of hematite (alpha-Fe2o3), maghemite (gamma-Fe2o3), magnetite (Fe3o4), goethite (alpha-Feooh), and lepidocrocite (famma-Feooh), *J. Geophys. Res.*, *90*(Nb4), 3126–3144, doi:10.1029/JB090iB04p03126.
Morris, R. V., et al. (2016), Silic volcanism on Mars evidenced by tridymite in high-SiO_2 sedimentary rock at Gale crater, *Proc. Natl. Acad. Sci. U.S.A.*, *113*(26), doi:10.1073/pnas.1607098113.

Murchie, S. L., et al. (2009), A synthesis of Martian aqueous mineralogy after 1 Mars year of observations from the Mars Reconnaissance Orbiter, *J. Geophys. Res.*, *114*, E00D06, doi:10.1029/2009JE003342.
Murchie, S., et al. (2007), Compact reconnaissance Imaging Spectrometer for Mars (CRISM) on Mars Reconnaissance Orbiter (MRO), *J. Geophys. Res.*, *112*, E05S03, doi:10.1029/2006JE002682.
Nachon, M., et al. (2014), Calcium sulfate veins characterized by ChemCam/Curiosity at Gale crater, Mars, *J. Geophys. Res. Planets*, *119*, 1991–2016, doi:10.1002/2013JE004588.
Oshagan, A., C. S. Edwards, and B. L. Ehlmann (2014), A near-automated method to generate multi-image HiRISE mosaics, Eight International Conference on Mars.
Pelkey, S. M., et al. (2007), CRISM multispectral summary products: Parameterizing mineral diversity on Mars from reflectance, *J. Geophys. Res.*, *112*, E08S14, doi:10.1029/2006JE002831.
Piqueux, S., and P. Christensen (2009), A model of thermal conductivity for planetary soils: 2. Theory for cemented soils, *J. Geophys. Res.*, *114*, E09005, doi:10.1029/2008JE003308.
Piqueux, S., and P. R. Christensen (2011), Temperature-dependent thermal inertia of homogeneous Martian regolith, *J. Geophys. Res.*, *116*, E07004, doi:10.1029/2011JE003805.
Presley, M., and P. Christensen (1997a), Thermal conductivity measurements of particulate materials. 1. A review, *J. Geophys. Res.*, *102*(E3), 6535–6549, doi:10.1029/96JE03302.
Presley, M., and P. Christensen (1997b), Thermal conductivity measurements of particulate materials. 2. Results, *J. Geophys. Res.*, *102*(E3), 6551–6566, doi:10.1029/96JE03303.
Rampe, E. B., D. Ming, R. V. Morris, D. Blake, D. Vaniman, T. F. Bristow, S. J. Chipera, A. S. Yen, J. Grotzinger, and D. Des Marais (2016), Mineralogical and geochemical trends in a fluviolacustrine sequence in Gale Crater, Mars, 2016 Goldschmidt Conference.
Rice, M. S., E. Cloutis, J. Bell, D. Bish, B. Horgan, S. Mertzman, M. Craig, R. Renaut, B. Gautason, and B. Mountain (2013), Reflectance spectra diversity of silica-rich materials: Sensitivity to environment and implications for detections on Mars, *Icarus*, *223*(1), 499–533.
Scheinost, A. C., A. Chavernas, V. Barron, and J. Torrent (1998), Use and limitations of second-derivative diffuse reflectance spectroscopy in the visible to near-infrared range to identify and quantify Fe oxide minerals in soils, *Clay Miner.*, *46*(5), 528–536, doi:10.1346/Ccmn.1998.0460506.
Seelos, K. D., F. P. Seelos, C. E. Viviano-Beck, S. L. Murchie, R. E. Arvidson, B. L. Ehlmann, and A. A. Fraeman (2014), Mineralogy of the MSL Curiosity landing site in Gale Crater as observed by MRO/CRISM, *Geophys. Res. Lett.*, *41*, 4880–4887, doi:10.1002/2014GL060310.
Siebach, K. L., and J. P. Grotzinger (2014), Volumetric estimates of ancient water on Mount Sharp based on boxwork deposits, Gale Crater, Mars, *J. Geophys. Res. Planets*, *119*, 189–198, doi:10.1002/2013JE004508.
Siebach, K. L., J. P. Grotzinger, L. C. Kah, K. M. Stack, M. Malin, R. Leveille, and D. Y. Sumner (2014), Subaqueous shrinkage cracks in the Sheepbed mudstone: Implications for early fluid diagenesis, Gale Crater, Mars, *J. Geophys. Res. Planets*, *119*, 1597–1613, doi:10.1002/2014JE004623.
Silvestro, S., D. A. Vaz, R. C. Ewing, A. P. Rossi, L. K. Fenton, T. I. Michaels, J. Flahaut, and P. E. Geissler (2013), Pervasive aeolian activity along rover Curiosity's traverse in Gale Crater, Mars, *Geology*, *41*(4), 483–486, doi:10.1130/G34162.1.
Stack, K. M., et al. (2014), Diagenetic origin of nodules in the Sheepbed member, Yellowknife Bay formation, Gale Crater, Mars, *J. Geophys. Res. Planets*, *119*, 1637–1664, doi:10.1002/2014je004617.
Stack, K. M., et al. (2016), Comparing orbiter and rover image-based mapping of an ancient sedimentary environment, Aeolis Palus, Gale Crater, Mars, *Icarus*, 1-19, doi:10.1016/j.icarus.2016.02.024, in press.
Swayze, G. A., et al. (2007), Spectral evidence for hydrated volcanic and/or impact glass on Mars with MRO CRISM, 7th International Conference on Mars, abstract #3384.
Thomson, B. J., N. T. Bridges, R. Milliken, A. Baldridge, S. J. Hook, J. K. Crowley, G. M. Marion, C. R. de Souza, A. J. Brown, and C. M. Weitz (2011), Constraints on the origin and evolution of the layered mound in Gale Crater, Mars using Mars Reconnaissance Orbiter data, *Icarus*, *214*(2), 413–432, doi:10.1016/j.icarus.2011.05.002.
Vaniman, D. T., et al. (2014), Mineralogy of a mudstone at Yellowknife Bay, Gale Crater, Mars, *Science*, *343*(6169), doi:10.1126/science.1243480.
Viviano-Beck, C. E., et al. (2014), Revised CRISM spectral parameters and summary products based on the currently detected mineral diversity on Mars, *J. Geophys. Res. Planets*, *119*, 1403–1431, doi:10.1002/2014JE004627.
Watkins, J. A., J. Grotzinger, N. Stein, S. G. Banham, S. Gupta, D. Rubin, K. Stack, and K. Edgett (2016), Paleotopography of erosional unconformity, base of Stimson formation Gale Crater, Mars, 47th Lunar and Planetary Science Conference.
Wellington, D. F., J. F. Bell, J. R. Johnson, K. M. Kinch, M. Rice, C. Hardgrove, and A. Godber (2015), Insights into the mineralogic diversity of lower Mount Sharp units from Mars Science Laboratory Mastcam multispectral observations, AGU Fall Meeting.
Wray, J. J. (2013), Gale Crater: The Mars Science Laboratory/Curiosity Rover landing site, *Int. J. Astrobiol.*, *12*(1), 25–38, doi:10.1017/S1473550412000328.
Yen, A. S., et al. (2016), Cementation and aqueous alteration of a sandstone unit under acidic conditions in Gale Crater, Mars, 47th Lunar and Planetary Science Conference.
Zolotov, M., and M. Mironenko (2007), Timing of acid weathering on Mars: A kinetic-thermodynamic assessment, *J. Geophys. Res.*, *112*, E07006, doi:10.1029/2006JE002882.